Available online at www.sciencedirect.com
ScienceDirect
International Journal of Multiphase Flow 33 (2007) 1337–1364
International Journal of Multiphase Flow
www.elsevier.com/locate/ijmulflow

Accurate numerical estimation of interphase momentum transfer in Lagrangian–Eulerian simulations of dispersed two-phase flows

R. Garg [a], C. Narayanan [b,1], D. Lakehal [b,1], S. Subramaniam [a,*]

[a] Department of Mechanical Engineering, H.M. Black Engineering, Iowa State University, Ames, IA 50011, USA
[b] Institute of Energy Technology, Swiss Federal Institute of Technology, CH-8092 Zurich, Switzerland

Abstract

The Lagrangian–Eulerian (LE) approach is used in many computational methods to simulate two-way coupled dispersed two-phase flows. These include averaged equation solvers, as well as direct numerical simulations (DNS) and large-eddy simulations (LES) that approximate the dispersed-phase particles (or droplets or bubbles) as point sources. Accurate calculation of the interphase momentum transfer term in LE simulations is crucial for predicting qualitatively correct physical behavior, as well as for quantitative comparison with experiments. Numerical error in the interphase momentum transfer calculation arises from both forward interpolation/approximation of fluid velocity at grid nodes to particle locations, and from backward estimation of the interphase momentum transfer term at particle locations to grid nodes. A novel test that admits an analytical form for the interphase momentum transfer term is devised to test the accuracy of the following numerical schemes: (1) fourth-order Lagrange Polynomial Interpolation (LPI-4), (3) Piecewise Cubic Approximation (PCA), (3) second-order Lagrange Polynomial Interpolation (LPI-2) which is basically linear interpolation, and (4) a Two-Stage Estimation algorithm (TSE). A number of tests are performed to systematically characterize the effects of varying the particle velocity variance, the distribution of particle positions, and fluid velocity field spectrum on estimation of the mean interphase momentum transfer term. Numerical error resulting from backward estimation is decomposed into statistical and deterministic (bias and discretization) components, and their convergence with number of particles and grid resolution is characterized. It is found that when the interphase momentum transfer is computed using values for these numerical parameters typically encountered in the literature, it can incur errors as high as 80% for the LPI-4 scheme, whereas TSE incurs a maximum error of 20%. The tests reveal that using multiple independent simulations and higher number of particles per cell are required for accurate estimation using current algorithms. The study motivates further testing of LE numerical methods, and the development of better algorithms for computing interphase transfer terms.

PACS: 47.61.Jd; 47.55.Kf

Keywords: Lagrangian–Eulerian; Numerical simulation; Two-way coupling; Numerical error; Statistical error; Particle method

* Corresponding author. Tel.: +1 515 294 369; fax: +1 515 294 3621.
E-mail address: shankar@iastate.edu (S. Subramaniam).
[1] Present address: ASCOMP GmbH, Zurich, Switzerland.

0301-9322/$ - see front matter © 2007 Elsevier Ltd. All rights reserved.
doi:10.1016/j.ijmultiphaseflow.2007.06.002

1. Introduction

The Lagrangian–Eulerian (LE) approach is widely used to simulate dispersed two-phase flows. This work focuses on the development of accurate numerical methods for computing the interphase momentum exchange term in LE simulations of two-phase flows with non-negligible mass loading. Therefore, the findings of this study are relevant to two-phase flows that must account for two-way coupling. Numerical error incurred in estimating the interphase momentum transfer term directly affects the fluid velocity solution, and feeds back to the particle trajectories. These errors can drastically affect the physical picture that emerges from an LE simulation. The conclusions of this study can also be easily generalized to the mass and energy interphase exchange terms.

1.1. Physical system

In the LE approach the dispersed phase consisting of N_p physical particles[2] is represented in a Lagrangian frame at time t by $\{\mathbf{X}^{(i)}(t), \mathbf{V}^{(i)}(t), i = 1, \ldots, N_p(t)\}$, where $\mathbf{X}^{(i)}$(t) denotes the ith particle's position and $\mathbf{V}^{(i)}$(t) represents its velocity. For the sake of simplicity we consider monodisperse particles here, although the conclusions of this work hold for polydisperse systems also. For monodisperse particles with diameter D_p, the particle mass is the same for each particle $m^{(i)} = m_p = \rho_p V_p$, where ρ_p and $V_p = \pi D_p^3/6$ are the individual particle density and volume respectively. The position and velocity of the physical particles evolve by

$$\frac{\mathrm{d}\mathbf{X}^{(i)}}{\mathrm{d}t} = \mathbf{V}^{(i)}, \tag{1}$$

$$m_p \frac{\mathrm{d}\mathbf{V}^{(i)}}{\mathrm{d}t} = \mathbf{f}^{(i)}, \quad i = 1, \ldots, N_p(t), \tag{2}$$

where $\mathbf{f}^{(i)}$ is the instantaneous force acting on the ith physical particle.

For the case of volumetrically dilute flows[3] with finite mass loading, the momentum conservation in the fluid phase is the single-phase momentum conservation equation augmented by an interphase momentum transfer term $\mathbf{F}^{fp}$, which accounts for the coupling of the dispersed-phase momentum with the fluid phase:

$$\rho_f \left(\frac{\partial \mathbf{U}^f}{\partial t} + \mathbf{U}^f \cdot \nabla \mathbf{U}^f \right) = \nabla \cdot \boldsymbol{\tau} - \mathbf{F}^{fp}. \tag{3}$$

This general formulation of the LE approach subsumes the application of the LE method to dispersed two-phase flows in three different simulation contexts: (1) direct numerical simulation (DNS) using a point-particle approximation for the dispersed phase, (2) large-eddy simulation (LES), and (3) computational fluid dynamics (CFD) using averaged equations for the carrier flow. The specific equations appropriate to each of these simulation methods can be recovered by appropriate interpretation (realization, filtered realization or statistical average) of the fluid velocity field, stress tensor and interphase momentum transfer term. Table 1 lists the representation of the carrier flow field and dispersed phase for these three simulation methods. This paper focuses primarily on accurate estimation of the interphase momentum transfer term $\mathbf{F}^{fp}(\mathbf{x}, t)$ in the context of CFD, where both fluid and particle phases are represented in a statistically averaged sense. However, the conclusions of this paper are equally applicable and relevant to the hybrid simulations DNS$^{(b)}$ and LES$^{(b)}$ in Table 1.

The equation for conservation of mean momentum in the fluid phase is obtained by ensemble averaging (Drew and Passman, 1998)

$$\rho_f \alpha_f \left(\frac{\partial \langle \mathbf{U}^f \rangle}{\partial t} + \langle \mathbf{U}^f \rangle \cdot \nabla \langle \mathbf{U}^f \rangle \right) = \nabla \cdot \langle \boldsymbol{\tau} \rangle - \langle \mathbf{F}^{fp} \rangle + \nabla \cdot \boldsymbol{\tau}^{RS}, \tag{4}$$

[2] By particle we mean any dispersed-phase element, including solid particles, droplets and bubbles.

[3] This assumption does not pose an inherent limitation on our investigation, but we choose this case to simplify the equations. The conclusions of this work will also hold for non-dilute cases but volume displacement effects will need to be accounted for.

Table 1
Representation of carrier flow and dispersed phase in different LE simulations: $DNS^{(b)}$ and $LES^{(b)}$ are denoted hybrid simulations

Simulation method	Carrier flow fields: $\mathbf{U}^{f}(\mathbf{x},t),\ p(\mathbf{x},t)$	Dispersed phase: $\{\mathbf{X}^{(i)}(t),\mathbf{V}^{(i)}(t), i=1,\ldots,N_p(t)\}$
$DNS^{(a)}$ with physical particles	Realization	Realization: point field
$DNS^{(b)}$ with stochastic particles	Realization	Statistically averaged density
$LES^{(a)}$ with physical particles	Filtered field of a realization	Spatially filtered point field
$LES^{(b)}$ with stochastic particles	Filtered field of a realization	Spatially filtered density
CFD	Mean fields	Statistically averaged density

where α_f is the average fluid volume fraction, ρ_f is the thermodynamic density of the fluid phase (assumed constant), $\boldsymbol{\tau}^{RS}$ is the residual stress resulting from ensemble averaging, and the angle brackets represent phasic averages of the terms.

Based on a statistical representation of the dispersed phase as a point process (Subramaniam, 2000, 2001) one can associate a density $f(\mathbf{x},\mathbf{v},t)$ with the ensemble of realizations $\{\mathbf{X}^{(i)}(t),\mathbf{V}^{(i)}(t), i=1,\ldots,N_p(t)\}$. The density $f(\mathbf{x},\mathbf{v},t)$ admits a decomposition

$$f(\mathbf{x},\mathbf{v},t) = n(\mathbf{x},t) f^{c}_{\mathbf{V}}(\mathbf{v}|\mathbf{x};t), \tag{5}$$

where $f^{c}_{\mathbf{V}}(\mathbf{v}|\mathbf{x};t)$ is the pdf of particle velocity conditional on physical space and $n(\mathbf{x},t)$ is the density of expected number of particles in physical space. In this notation $\mathbf{v}$ is the sample space variable corresponding to particle velocity $\mathbf{V}$. The expected value of the interphase momentum transfer term (or fluid–particle interaction force) $\mathbf{F}^{fp}(\mathbf{x},t)$ can be written as an integral over velocity space:

$$\langle \mathbf{F}^{fp}\rangle(\mathbf{x},t) = \int_{[\mathbf{v}]} \langle \mathbf{f}|\mathbf{x},\mathbf{v};t\rangle n(\mathbf{x},t) f^{c}_{\mathbf{V}}(\mathbf{v}|\mathbf{x};t)\,\mathrm{d}\mathbf{v}, \tag{6}$$

where $\langle \mathbf{f}|\mathbf{x},\mathbf{v};t\rangle$ is the conditional average of the force acting on the physical particles. It is this quantity that we seek to calculate accurately in our study. Since we only refer to average fluid velocity and average interphase momentum transfer from here on, to improve readability the angle bracket notation is omitted from these quantities in the rest of the paper.

1.2. Computational representation

In LE simulations the dispersed-phase density $f(\mathbf{x},\mathbf{v},t)$ is indirectly represented by N_c computational particles at time t in a Lagrangian frame by $\{\mathbf{X}^{*(i)}(t),\mathbf{V}^{*(i)}(t), i=1,\ldots,N_c(t)\}$, with $\mathbf{X}^{*(i)}(t)$ denoting the ith computational particle's position and $\mathbf{V}^{*(i)}(t)$ its velocity. The number of computational particles N_c does not necessarily have to equal the number of physical particles N_p, which in our point process model is a random number. Typically N_c is chosen to be smaller than N_p by even orders of magnitude sometimes, and the correspondence between the computational representation and the physical system is enforced in the following statistical sense.

The number of physical particles represented by the ith computational particle is denoted by $n_p^{(i)}$, such that the sum over all the computational particles is equal to the expected number of physical particles

$$\sum_{i=1}^{N_c} n_p^{(i)} = \langle N_p\rangle. \tag{7}$$

Therefore, the statistical weight assigned to each computational particle is

$$\mu^{(i)} = \frac{n_p^{(i)}}{\sum_{i=1}^{N_c} n_p^{(i)}} = \frac{n_p^{(i)}}{\langle N_p\rangle}, \tag{8}$$

which satisfies the normalization property $\sum_{i=1}^{N_c}\mu^{(i)} = 1$.

The position and velocity of each computational particle evolve by the equations

$$\frac{\mathrm{d}\mathbf{X}^{*(i)}}{\mathrm{d}t} = \mathbf{V}^{*(i)}, \tag{9}$$

$$m_{\mathrm{p}}\frac{\mathrm{d}\mathbf{V}^{*(i)}}{\mathrm{d}t}=\mathbf{f}^{*(i)},\quad i=1,\ldots,N_{\mathrm{c}}(t), \tag{10}$$

where $\mathbf{f}^{*(i)}$ is the *modeled* force acting on the ith computational particle. The computational particle position $\mathbf{X}^{*(i)}$ and velocity $\mathbf{V}^{*(i)}$ are evolved in time from initial conditions at time t_0 that correspond to a specified initial number density $n(\mathbf{x},t_0)$ and velocity probability density function $f_{\mathbf{V}}^{c}(\mathbf{v}|\mathbf{x};t_0)$ of the physical particles.

A general form of the particle force model that subsumes different drag force correlations is

$$\mathbf{f}^{*(i)}(t)=\mathbf{f}\left(\mathbf{U}^{\mathrm{f}}(\mathbf{X}^{*(i)}(t),t),\mathbf{V}^{*(i)},\rho_{\mathrm{f}},v_{\mathrm{f}},\rho_{\mathrm{p}},D_{\mathrm{p}}\right), \tag{11}$$

where ρ_{f} and v_{f} is the fluid phase density and kinematic viscosity, respectively. A more general force model could include additional terms such as the added mass term, Basset history term, or Saffman lift, as dictated by the problem physics. Even though we only model the drag in our study, our conclusions regarding the accurate numerical calculation of the interphase momentum transfer term will apply to this wider class of flows, with minor modifications to account for the changes in the functional form $\mathbf{f}$ that will be necessitated by the additional physics.

1.3. Problem statement

Proper representation of the flow physics in an LE simulation is contingent upon accurate calculation of the mean interphase momentum transfer term $\mathbf{F}_{\mathrm{fp}}(\mathbf{x},t)$ from the LE solution, i.e., the mean fluid velocity field $\mathbf{U}^{\mathrm{f}}(\mathbf{x},t)$, and the position and velocity of the computational particles $\{\mathbf{X}^{*(i)}(t),\mathbf{V}^{*(i)}(t),i=1,\ldots,N_{\mathrm{c}}\}$. The mean interphase momentum transfer term $\mathbf{F}_{\mathrm{fp}}(\mathbf{x},t)$ at Eulerian grid nodes is estimated from this solution data in two steps:

(1) *Calculation of particle forces* $\mathbf{f}^{*(i)}$: This requires calculation of the fluid velocity at the particle location $\mathbf{U}^{\mathrm{f}}(\mathbf{X}^{*(i)},t)$ in Eq. (11) from the fluid velocity at Eulerian grid nodes. The numerical estimate of the fluid velocity field $\mathbf{U}^{\mathrm{f}}(\mathbf{x},t)$ at the particle location $\mathbf{X}^{*(i)}$ using a representation of $\mathbf{U}^{\mathrm{f}}$ at M grid nodes is denoted $\left\{\mathbf{U}^{\mathrm{f}}(\mathbf{X}^{*(i)},t)\right\}_M$, and is obtained through *forward interpolation/approximation* as

$$\left\{\mathbf{U}^{\mathrm{f}}(\mathbf{X}^{*(i)},t)\right\}_M=\mathscr{F}\{\mathbf{U}^{\mathrm{f}}_m,m=1,\ldots,M;\mathbf{X}^{*(i)}\}, \tag{12}$$

where the fluid velocity at the mth Eulerian grid node is denoted $\mathbf{U}^{\mathrm{f}}_m$, and $\mathscr{F}$ is a generic interpolation/approximation operation. The particle force $\mathbf{f}^{*(i)}$ is then obtained by substituting $\left\{\mathbf{U}^{\mathrm{f}}(\mathbf{X}^{*(i)},t)\right\}_M$ for $\mathbf{U}^{\mathrm{f}}(\mathbf{X}^{*(i)},t)$ in Eq. (11).

(2) *Mean interphase momentum transfer* $\mathbf{F}_{fp}(\mathbf{x},t)$ *from particle forces* $\mathbf{f}^{*(i)}$: The numerical procedure to calculate the Eulerian mean field $\mathbf{F}_{fp}(\mathbf{x},t)$ from particle data $\{\mathbf{X}^{*(i)}(t),\mathbf{f}^{*(i)}(t),i=1,\ldots,N_{\mathrm{c}}\}$ is describe variously as mean estimation from particle data, projection of fluid–particle interaction forces onto the Eulerian grid, or backward estimation. The numerical estimate for the mean interphase momentum transfer $\mathbf{F}_{\mathrm{fp}}(\mathbf{x},t)$ at the mth Eulerian grid node is denoted $\{\mathbf{F}^{\mathrm{fp}}_m\}$, and the general form of its estimate from the particle data is

$$\{\mathbf{F}^{\mathrm{fp}}_m\}=\mathscr{E}\{\mathbf{X}^{*(i)},\mathbf{f}^{*(i)},n^{(i)}_{\mathrm{p}},i=1,\ldots,N_{\mathrm{c}}(t)\}, \tag{13}$$

where $\mathscr{E}$ like $\mathscr{F}$ is another generic interpolation/approximation operator.

1.4. Review of existing schemes

Both forward interpolation and the estimation of mean fields from particle data have been studied by other researchers, and a selective review that motivates this study follows.

1.4.1. Forward interpolation

Yeung and Pope (1988) investigated many numerical approaches for interpolation of fluid velocity at a Lagrangian particle location in homogeneous turbulence. Among the schemes they considered are a trilinear scheme, a 13-point third-order scheme based on Taylor series (TS-13), and a fourth-order cubic spline. Their

study shows that the fourth-order spline is most accurate for forward interpolation, followed by the TS-13 scheme. The trilinear interpolation scheme was found to be unacceptably poor. Balachandar and Maxey (1989) also analyzed various numerical schemes to calculate the fluid velocity at a particle location in one-way coupled spectral simulations of decaying homogeneous turbulence by comparing them with the most accurate, and also the most computationally expensive, direct summation (DS) scheme. They studied the TS-13 scheme, sixth-order Lagrangian interpolation (LPI-6), partial Hermite interpolation (PHI), shape function method (SFM), and linear interpolation (LPI-2). They find that the estimation of statistical quantities such as Lagrangian velocity correlation, effective eddy diffusivity, and mean square particle dispersion are not sensitive to the approximation scheme used. They show that on a 32^3 grid size at low Reynolds number ($Re_\lambda = 17$) the LPI-6 scheme is sufficient to accurately extract quantities such as absolute velocity of single particle and also the relative velocity of two particles. However, at higher Reynolds number ($Re_\lambda = 26.5$) the more accurate PHI scheme is needed, at additional computational expense. It should be noted that the TS-13 scheme is best suited to simulations of homogeneous turbulence that incorporate a de-aliasing procedure and make use of staggered grid. The PHI and SFM schemes have been developed specifically for spectral simulation. While these studies provide useful guidelines to choose appropriate schemes for forward interpolation, they only address the first step in accurate estimation of the mean interphase momentum transfer term.

1.4.2. Estimation of mean field from particle data

Various approaches have been proposed for the second step that involves estimation of the mean interphase momentum transfer term $\mathbf{F}_m^{\mathrm{fp}}$ from particle data $\{\mathbf{X}^{*(i)}(t), \mathbf{f}^{*(i)}(t), i = 1, \ldots, N_c\}$. We review three principal approaches here: (1) the particle-in-cell (PIC) method, (2) the projection onto neighboring nodes (PNN) method, and (3) the projection onto identical stencil (PIS) method.

PIC: Crowe (1982) extended the particle-in-cell (PIC) method (Evans and Harlow, 1957; Harlow, 1988) to calculate the mean interphase momentum transfer term. In this method, the mean interphase momentum transfer term is calculated as the summation of forces $\mathbf{f}^{*(i)}$ exerted on the fluid by each particle in the control volume surrounding a grid node as shown in Fig. 1a and also expressed by Eq. (A.1). This is effectively a box kernel, which has the disadvantage that its estimate is piecewise-constant in physical space (Pope, 2000). Therefore this method cannot be used to calculate gradients of the mean interphase momentum transfer field, if they are needed.

PNN: This is a so-called projection method wherein rather than summing all the particle forces around a grid node, each particle force is projected onto the neighboring grid points (eight in 3-D, four in 2-D) based on a weighting scheme (see Fig. 1b). The weights can be based on the cell volumes as in Squires and Eaton (1990), or on the distance between the particle and the node as used by Elghobashi and Truesdell (1993). The expression for estimation by PNN method based on the distance between particle and the node is given by Eq. (A.3).

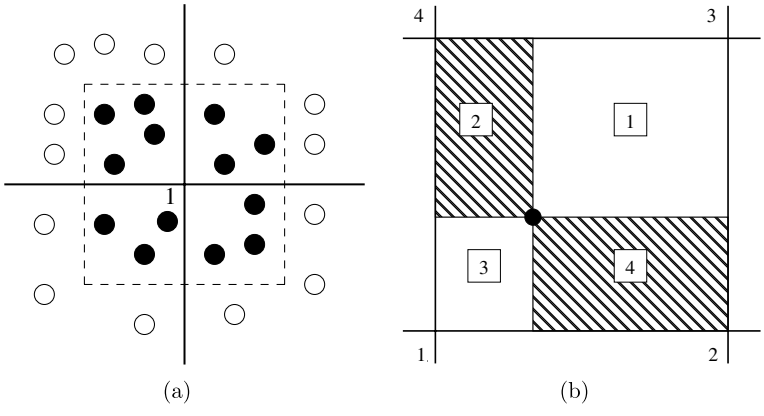

Fig. 1. Sketch showing the PIC and PNN mean estimation schemes: (a) Mean estimation by PIC method in 2-D. Grid node 1 receives the full contribution from particles (shown as black spheres) located in cell area (shown by dotted lines) around it. (b) Mean estimation by PNN method in 2-D. For a particle (shown as a black sphere) in a two-dimensional cell, grid node 1 receives a fraction of the particle force which is proportional to the area of region 1 divided by the entire cell area.

Boivin et al. (1998) compared PIC and PNN methods by first forward-interpolating a turbulent velocity field specified at Eulerian grid nodes to randomly generated off-grid particle locations using a third-order LPI scheme. These interpolated fluid velocities at the particle locations are then used as particle data to estimate the fluid velocity field at the Eulerian grid nodes using PIC and PNN. Their test results show that the PNN scheme results in a fluid velocity spectrum that is closer to the original velocity field spectrum field than that obtained using the PIC method. However, the conclusions of the Boivin study need to be interpreted carefully because their test is significantly different from our problem of mean interphase momentum transfer estimation in many respects. Since the Boivin et al. (1998) study only tries to recover the fluid velocity field instead of the interphase momentum transfer term (cf. Eq. (11)), it is not affected by the particle velocity $\mathbf{V}^{*(i)}$ or its pdf $f^c_{\mathbf{V}}(\mathbf{v}|\mathbf{x};t)$. Boivin et al. randomly assign only one particle location to each cell. As is shown later in this paper, this results in an unacceptably high level of statistical error.

PIS: Sundaram and Collins (1996) show that in order to ensure overall energy balance, the order of the interpolation scheme used in the forward interpolation should be the same as that used in the backward estimation. We noted earlier in this paper that the studies on forward interpolation reveal that at least for turbulent velocity fields in DNS, high-order schemes like TS-13 or LPI-6 are needed for accuracy. These high-order schemes have broad stencils in physical space that extend well beyond the cell where the particle is present. A PIS scheme will then require a weighting kernel with identically broad support to compute the mean interphase momentum transfer from particle forces. Each particle exerts a non-local influence on the estimate of the interphase momentum transfer, and this raises a concern whether the numerics is consistent with the flow physics. Using a fourth-order LPI scheme for both forward interpolation and backward estimation (in Eqs. (A.2) and (A.3), respectively) on coarse and fine grid resolution, they note that the result of spreading particle influence over a large volume does not significantly affect the dynamics of the mean energy in a particle-laden turbulent flow. On this basis, Sundaram and Collins (1996) assert that the PIS symmetry in the order of the scheme used for both forward interpolation and backward estimation is required, even if it increases the domain of influence of each particle due to a broad interpolation stencil.

Narayanan et al. (2002) assess the relative merits of the PNN and PIS methods by comparing the growth rates of mixing layers obtained using LE simulations with these schemes, to those obtained from a linear stability analysis. However, the results obtained for growth rates are too close to draw any conclusions about the relative merits of the two methods.

In all LE numerical implementations, including those cited above, there are two numerical parameters: the number of Eulerian grid cells and the number of computational particles. The estimate for the mean interphase momentum transfer term $\mathbf{F}^{\mathrm{fp}}$ on an Eulerian grid is obtained from a finite number of particle forces $\mathbf{f}^*$. This leads to *statistical error*, which can only be eliminated in the limit of infinite particles (also called the dense data limit). This limit is only asymptotically approached by simulations with a very large number of particles, and such calculations are expensive. Typical LE simulations must be reasonably accurate in a range of finite number of particles. A finite number of grid cells also leads to *spatial discretization error* as in CFD of single-phase flow. Numerical schemes in the LE context need to balance statistical and spatial discretization error.

In spite of the considerable work on forward interpolation as well as projection methods (PIC, PNN, PIS), there is no comprehensive study that quantifies the spatial and statistical error resulting from numerical estimation of mean interphase momentum transfer. The conclusions of Boivin et al. (1998) are based on a single test with 96^3 particles that does not quantify the statistical error, or its scaling with the number of particles. The Sundaram and Collins (1996) study tests only the fourth-order LPI scheme and does not quantify spatial and statistical error. Narayanan et al. (2002) consider LPI schemes of different orders but they do not characterize the behavior of spatial or statistical error. Lakehal and Narayanan (2003) quantify the effect of varying the total number of particles in an LE simulation on calculation of the average interfacial force. They find that increasing the number of particles shows a reduction in statistical noise, and the estimated interfacial force tends to an asymptotic value. However, this study also does not decompose the error into deterministic and statistical components. Also while numerical convergence with number of particles is empirically demonstrated, the accuracy of the scheme is not quantified. Are et al. (2005) investigate only spatial discretization error by considering the limit of dense data (1 billion particles).

In this work we construct a test problem for which the interphase momentum transfer term can be calculated analytically. We then compare the numerical error incurred by four different schemes in estimation of the

mean interphase momentum transfer term. The total numerical error is decomposed into statistical and deterministic components. Statistical error is defined as the fluctuations in interphase force estimation that arise as a result of finite particles. Deterministic error, which is further decomposed into bias and discretization components, results from finite number of particles and grid size, respectively. The individual contributions to the total numerical error from finite number of particles (statistical error and bias error) and finite grid size (spatial discretization error) are identified. The behavior of statistical error, bias error, and spatial discretization error is characterized over a range of grid sizes and total number of particles.

The four numerical schemes for calculation of the mean interphase momentum transfer term that are considered in this work are:

(1) *LPI-4*: This is a fourth-order Lagrange polynomial interpolation (LPI) which has been widely used for both forward and reverse interpolation (Sundaram and Collins, 1996; Narayanan et al., 2002; Sundaram and Collins, 1999). It is a true interpolation scheme because it recovers the specified values of fluid velocity at grid nodes. The LPI-4 basis functions are shown in Fig. 2a. Since this scheme is fourth-order accurate (Conte and Boor, 1980), in forward interpolation the error incurred using LPI-4 should exhibit fourth-order convergence with respect to grid spacing for a uniform grid. The LPI-4 stencil is four grid cells wide, as shown in Fig. 2a. In backward estimation also its kernel bandwidth is four grid cells wide. The kernel bandwidth determines the extent to which Lagrangian particle data is smeared on the Eulerian flow grid in backward estimation.

(2) *PCA*: This scheme has piecewise continuous cubic polynomial basis functions that are similar to the kernel derived by Monaghan and Lattanzio (1985) based on B-spline functions. See Fig. 2b for the PCA basis functions. It is important to note that this is not standard cubic spline interpolation that involves a matrix solution for the spline coefficients. In fact, this is only a piecewise cubic *approximation* that does not exactly recover specified values of the velocity field at the grid nodes. To distinguish it from the standard cubic spline interpolation, this scheme is referred to as piecewise cubic approximation (PCA). Monaghan (1992) notes that this scheme is only second-order accurate, in contrast to cubic spline interpolation which is fourth-order accurate. In backward estimation its kernel bandwidth is four grid cells wide.

(3) *LPI-2*: This is a second-order Lagrange polynomial interpolation scheme, which is essentially a trilinear interpolation scheme that is identical to the PNN method (Squires and Eaton, 1990; Elghobashi and Truesdell, 1993; Boivin et al., 1998). It is a true interpolation scheme that is formally second-order accurate for forward interpolation. In backward estimation its kernel bandwidth is two grid cells wide.

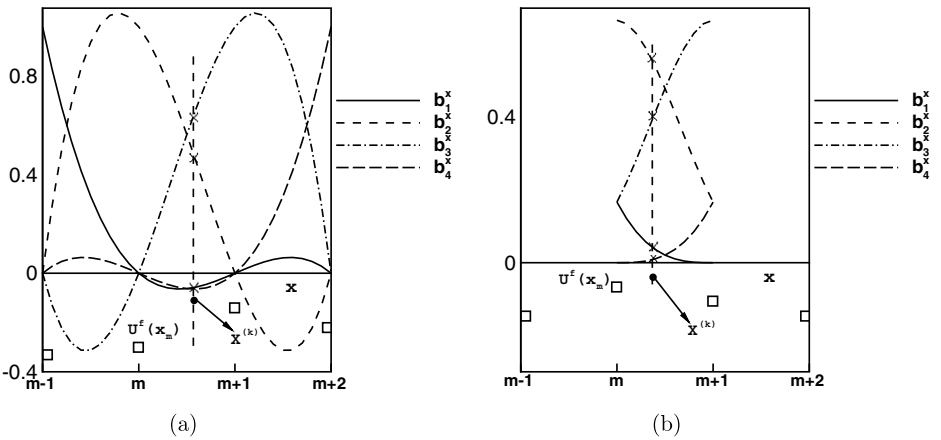

Fig. 2. (a) Basis functions for LPI-4. (b) Basis functions for PCA. In both figures, squares represent the fluid velocity at that grid node, $X^{(k)}$ is the location of particle (shown by black sphere) located between nodes m and $m+1$. The intersections of the vertical dashed line with the curves (shown by crosses) indicates the value of the basis function at $X^{(k)}$ that multiplies the nodal fluid velocity in Eq. (A.2) to compute the fluid velocity at $X^{(k)}$.

(4) *TSE*: This two-stage estimation algorithm is developed by Dreeben and Pope (1992). It is useful in simulations that involve unstructured meshes (Subramaniam and Haworth, 2000). For forward interpolation it is identical to LPI-2, and is formally second-order accurate. For backward estimation it employs a grid-free two-stage algorithm. In the first stage, it estimates weighted values of the particle property using a linear kernel of user-specified bandwidth (e.g., interphase force) at knot locations that depend on where the particles are located. The second stage involves least-squares fitting of locally linear or quadratic functions to these knot values. The advantage of this method is that its convergence characteristics are not tied to the Eulerian grid (in fact it does not need an Eulerian grid at all!), but by adjusting the bandwidth of the kernel the user can balance the contribution from truncation and statistical errors.

For complete details of the interpolation schemes, the reader is referred to Appendix A.

2. Test problem

We consider a simple physical problem to examine the numerical convergence and accuracy of the four schemes in calculating the mean interphase momentum transfer term. The physical system is a volumetrically dilute particle-laden flow with large particle to fluid density ratio ($\rho_p \gg \rho_f$). The solid particles are monodisperse and small compared to the smallest flow length scale, but large enough so Brownian motion of the particles can be neglected. The Reynolds number for relative motion between the particle and the fluid is $\mathcal{O}(1)$. Under these conditions the interphase momentum transfer is due to drag and buoyancy forces. If we neglect buoyancy and assume a linear drag model (which is valid for Reynolds number $\mathcal{O}(1)$), the modeled particle force $\mathbf{f}^{*(i)}$ is given by

$$\mathbf{f}^{*(i)} = m_p \frac{\mathbf{U}^f\left(\mathbf{X}^{*(i)}\right) - \mathbf{V}^{*(i)}}{\tau_p}, \tag{14}$$

where $\tau_p = \rho_p D_p^2/(18\nu_f\rho_f)$ is the particle momentum response time. In this test we do not consider time evolution, but simply evaluate the mean interphase momentum transfer term at some fixed time instant t. Therefore the time dependence is omitted in the rest of the description of this static test.

We consider a statistically homogeneous problem where the particle velocity distribution is independent of physical location $\mathbf{x}$, so that $f^c_{\mathbf{V}}(\mathbf{v}|\mathbf{x}) = f_{\mathbf{V}}(\mathbf{v})$. If the particle density in physical space $f_{\mathbf{X}}(\mathbf{x}) = n(\mathbf{x})/\langle N_p\rangle$ is known, then Eq. (6) simplifies to

$$\langle \mathbf{F}^{fp}\rangle(\mathbf{x}) = \langle N_p\rangle \int_{[\mathbf{v}]} \langle \mathbf{f}|\mathbf{x},\mathbf{v}\rangle f_{\mathbf{X}}(\mathbf{x}) f_{\mathbf{V}}(\mathbf{v})\,\mathrm{d}\mathbf{v}. \tag{15}$$

If the mean fluid velocity field $\mathbf{U}^f(\mathbf{x})$ is specified, along with the particle position and velocity distributions, the final analytical expression for $\langle \mathbf{F}^{fp}\rangle$ from Eq. (15) is

$$\langle \mathbf{F}^{fp}\rangle(\mathbf{x}) = \frac{m_p\langle N_p\rangle}{\tau_p}\left[\mathbf{U}^f(\mathbf{x}) f_{\mathbf{X}}(\mathbf{x}) - \langle \mathbf{V}\rangle f_{\mathbf{X}}(\mathbf{x})\right]. \tag{16}$$

It is interesting to note that although in the above equation $\langle \mathbf{F}^{fp}\rangle$ is independent of the variance in particle velocity, numerical estimates for this quantity suffer from statistical noise which increases with particle velocity variance. The estimate of mean interphase momentum transfer term depends on (i) the mean fluid velocity field, (ii) the particle position distribution, and (iii) the particle velocity distribution.[4] The following specification of the mean fluid velocity field, and the particle position and velocity distribution define the baseline test

[4] Although the analytical value depends only on the mean particle velocity, the numerical estimate depends on the variance of the particle velocity distribution.

case, which we denote Test 1. The fluid velocity field $\mathbf{U}^{\mathrm{f}} = \{U_1^{\mathrm{f}}, 0, 0\}$ is chosen to be of a simple transcendental form

$$U_1^{\mathrm{f}}(x, y) = \cos\left(\frac{2\pi x}{\mathscr{L}_x}\right)\cos\left(\frac{2\pi y}{\mathscr{L}_y}\right), \tag{17}$$

in a domain $\mathscr{D} = [0, \mathscr{L}_x] \times [0, \mathscr{L}_y] \times [0, \mathscr{L}_z]$. The particle positions are randomly chosen according to a uniform distribution in the domain $\mathscr{D}$. The particle velocity $\mathbf{V} = \{V_1, 0, 0\}$ is specified by the distribution of V_1, which is chosen to be a Gaussian with unit mean and variance σ^2. For the baseline test the variance is chosen to be zero, which corresponds to a delta-function specification of the particle velocity distribution. Fig. 3 shows the contour plot of scaled analytical mean interphase momentum transfer term in the x-direction obtained from Eq. (16) for the baseline test case. This baseline test case is used to completely characterize the statistical error, bias error, and spatial discretization error for the four numerical schemes over a wide range of numerical parameter values.

We consider three variants of the baseline case in our tests to specifically probe certain other convergence characteristics of the numerical schemes used to estimate the mean interphase momentum transfer term. Unless noted otherwise, the problem parameters are retained at their baseline values. In the first variant (Test 2), a non-zero particle velocity variance is introduced to represent non-zero particle velocity fluctuations that can be expected in most practical two-phase flows. For the linear drag law considered here, this non-zero particle velocity variance manifests itself as statistical noise in the estimate of the mean interphase momentum transfer. This test assesses the capability of the various schemes to yield accurate estimates of the mean interphase momentum transfer term with finite computational particles for noisy data.

Tests 3 and 4 are variants of Test 2 that consider the effect of changing the particle position distribution and spectrum of the fluid velocity field, respectively. In these tests we only characterize the total error, but we do not identify individual contributions. In Test 3 we investigate the effect of a non-uniform distribution of physical particles while retaining the non-zero particle velocity variance in Test 2. If we do not introduce any computational particle number density control, the distribution of computational particles mimics that of the physical particles and we essentially generate non-uniform sampling. This test is representative of the spatial inhomogeneity in number density that is encountered in LE computations of real two-phase flows.

In Test 4, the effect of changing the spectrum of the fluid velocity field is investigated by changing the wavelength of the cosine waves in Eq. (17) (the non-zero particle velocity variance of Test 2 is retained). Our intent in performing this test is to characterize the applicability of the four schemes to CFD, LES$^{(b)}$ and DNS$^{(b)}$, each of which has progressively more high-wavenumber content in the velocity field. By changing the wavelength of the cosine waves on a fixed grid, we effectively vary the resolution of the velocity field, and investigate the consequences on the computed interphase momentum transfer term.

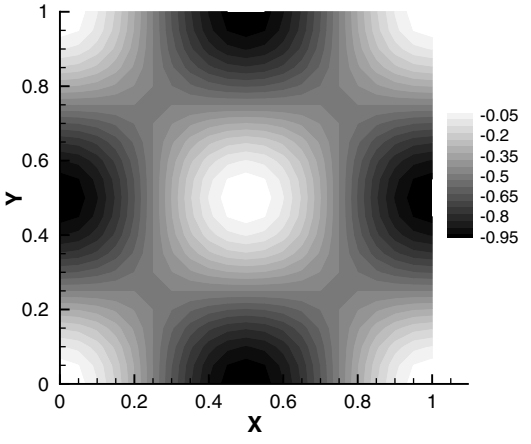

Fig. 3. Contour plot of scaled analytical mean interphase momentum transfer term $\langle F_x^{\mathrm{fp}}\rangle / \langle F_x^{\mathrm{fp}}\rangle_{\max}$ for the fluid velocity field given by Eq. (17) and mean particle velocity $\langle V_1\rangle = 1.0$.

3. Numerical analysis

In order to calculate a numerical estimate of $\langle \mathbf{F}^{\mathrm{fp}} \rangle(\mathbf{x})$, the physical domain $\mathscr{D}$ is discretized using a structured grid with $M_x \times M_y \times M_z$ cells. In all our tests the domain is a unit cube with $10 \leqslant M_x = M_y \leqslant 60$, and $M_z = 3$. Since the mean velocity field is only a function of (x, y), we use more grid cells in the x–y plane. The expected total number of physical particles $\langle N_{\mathrm{p}} \rangle$ is represented by N_{c} computational particles, with each computational particle representing $n_{\mathrm{p}} = \langle N_{\mathrm{p}} \rangle / N_{\mathrm{c}}$ physical particles, resulting in equal statistical weight $\mu = 1/N_{\mathrm{c}}$ for each computational particle. The average number of computational particles in a grid cell is denoted $N_{\mathrm{pc}} = N_{\mathrm{c}}/M$, where $M = M_x M_y M_z$ is the total number of grid cells. The numerical parameters affecting the accuracy of mean interphase momentum transfer term estimation are (i) the number of computational particles per cell N_{pc}, and (ii) grid size, which we represent by total number of nodes M.

The numerical estimate for $\mathbf{F}^{\mathrm{fp}}(\mathbf{x})$ at the mth grid node obtained from the above discretization (M cells and N_{pc} particles per cell) is written as

$$\{\mathbf{F}_m^{\mathrm{fp}}\}_{N_{\mathrm{pc}},M} = \frac{1}{V_m} \sum_{i=1}^{N_{\mathrm{c}}} \mathbf{f}^{*(i)} n_{\mathrm{p}}^{(i)} W(\mathbf{X}^{*(i)}, \mathbf{x}^m), \tag{18}$$

where W is a kernel having compact support that determines the influence of the particle force at a grid node located at $\mathbf{x}^m$, and V_m is the geometric volume of the mth grid cell. The reader is referred to Appendix A for complete details on the estimation procedure.

The error involved in the above estimate is composed of forward interpolation error and backward estimation error corresponding to steps 1 and 2 in Section 1.3, respectively. The forward interpolation error is a result of interpolating the fluid velocity that is known at M nodes to an arbitrary particle location $\mathbf{X}^{*(i)}$ using Eq. (A.2). This interpolated value is denoted $\{\mathbf{U}^{\mathrm{f}}(\mathbf{X}^{*(i)})\}_M$ (subscript M represents the number of grid nodes). A global rms forward interpolation error in estimating $\mathbf{U}_{\mathrm{f}}(\mathbf{X}^{*(i)})$ is defined as

$$\epsilon_U = \sqrt{\frac{\sum_{i=1}^{N_{\mathrm{c}}} \left(\{\mathbf{U}_{\mathrm{f}}(\mathbf{X}^{*(i)})\}_M - \mathbf{U}_{\mathrm{f}}(\mathbf{X}^{*(i)}) \right)^2}{N_{\mathrm{c}}}} \propto \frac{1}{M^p}, \tag{19}$$

which scales as M^{-p} with grid size, where the exponent p depends on the order of convergence of the numerical scheme. Although we use data from N_{c} particles to compute this error, the forward interpolation error scales purely with grid size (independent of number of particles). The error from forward interpolation is reported in Section 4.1.1.

In this study we are interested in characterizing the individual contributions to total numerical error in the estimate $\{\mathbf{F}_m^{\mathrm{fp}}\}_{N_{\mathrm{pc}},M}$ from forward interpolation (step 1) and backward estimation (step 2). In order to isolate and quantify the backward estimation error incurred by the four different schemes, we need the forward interpolation error to remain the same when forming the estimate $\{\mathbf{F}_m^{\mathrm{fp}}\}_{N_{\mathrm{pc}},M}$. This is achieved by exploiting the fact that the fluid velocity field is analytically specified by Eq. (17) in the entire domain. In the rest of the error analysis that follows for the numerical estimation of $\mathbf{F}^{\mathrm{fp}}(\mathbf{x}, t)$, it is assumed that the fluid velocity is obtained from the analytical expression and therefore, the error in the estimate arises only from backward estimation. In all the tests that report backward estimation errors (Section 4.1.2 through end of Section 4.2), the exact analytical expression for $\mathbf{U}^{\mathrm{f}}(\mathbf{X}^*)$ is used in Eq. (14) to calculate $\mathbf{f}^*$.

The numerical estimate $\{\mathbf{F}_m^{\mathrm{fp}}\}_{N_{\mathrm{pc}},M}$ is a random variable, and its difference from $\mathbf{F}^{\mathrm{fp}}(\mathbf{x})$ measured in p-norm defines the total numerical error:

$$\epsilon_F \equiv \| \{\mathbf{F}_m^{\mathrm{fp}}\}_{N_{\mathrm{pc}},M} - \langle \mathbf{F}_m^{\mathrm{fp}} \rangle \|_{\mathrm{p}}. \tag{20}$$

This total numerical error contains contributions from finite grid resolution and finite number of computational particles. Whereas in standard CFD finite-difference/finite-volume codes it is sufficient to reduce the grid size and time step to empirically establish numerical convergence, this difference in the dependence of the numerical error requires a new approach to establishing numerical convergence of LE calculations.

Many LE numerical studies employ the conventional CFD approach to establish numerical convergence. However, simply increasing the grid resolution by increasing M while keeping the total number of computa-

tional particles N_c fixed does not result in a monotonic decrease of the total error. This is because as M is increased for fixed N_c, the number of computational particles per cell $N_{pc} = N_c/M$ decreases. Decreasing N_{pc} means fewer samples per cell, and this results in higher statistical error (which characterizes the level of fluctuations in the random estimate $\{\mathbf{F}_m^{fp}\}_{N_{pc},M}$) for grid-based estimation methods. On the other hand, while decreasing the total number of cells M with fixed total number of computational particles does decrease the statistical error, it is at the cost of increasing spatial discretization error.

Most numerical studies seek to establish convergence of LE simulations by increasing the total number of particles N_c. For a fixed total number of particles there exists an optimal choice of grid size that minimizes the total numerical error. Clearly, a complete characterization of the individual contributions to total error from finite number of particles and finite grid size is essential to determine the optimal choice of numerical parameters for any scheme. This motivates an error decomposition that is described below.

3.1. Error decomposition

We decompose the numerical error using an approach similar to that employed by Xu and Pope (1999). For our test problem, only the x-component of the force contributes to the error in Eq. (20) which is decomposed as

$$\epsilon_F \equiv \{F_{x,m}^{fp}\}_{N_{pc},M} - \langle F_{x,m}^{fp}\rangle = \Sigma_F + D_F = \Sigma_F + B_F + S_F, \tag{21}$$

where Σ_F is the statistical error, and D_F is the deterministic error. The deterministic error D_F is further decomposed into bias B_F and discretization S_F error components.

The finite number of particles used in Eq. (18) to generate a random estimate of the mean interphase momentum transfer term $\{\mathbf{F}_m^{fp}\}_{N_{pc},M}$ results in statistical fluctuations of the estimate about its expected value. The statistical error Σ_F, arising from these fluctuations, is defined as

$$\Sigma_F \equiv \{\mathbf{F}_m^{fp}\}_{N_{pc},M} - \langle\{\mathbf{F}_m^{fp}\}_{N_{pc},M}\rangle. \tag{22}$$

The statistical error is assumed to follow a normal distribution, and is modeled as

$$\Sigma_F = \frac{c_F\theta}{\sqrt{N_{pc}}}, \tag{23}$$

where c_F is the statistical error coefficient and θ is a standardized normal random variable. Xu and Pope (1999) note in their calculations that the statistical error Σ_F converges as $N_{pc}^{-1/2}$ and an identical behavior has been seen in other PDF/Monte Carlo simulations (Pope, 1995; Welton et al., 1997). Clearly the statistical error decreases as the number of computational particles per cell N_{pc} increases, and for sufficiently high N_{pc} we expect c_F to be a constant independent of N_{pc}. As we shall see later, statistical error can also be decreased by performing multiple independent simulations (MIS) with the same nominal N_{pc} per simulation, and then averaging over the MIS.

The bias error B_F is defined as the deterministic error resulting from finite number of particles and is written as

$$B_F \equiv \langle\{\mathbf{F}_m^{fp}\}_{N_{pc},M}\rangle - \{\mathbf{F}_m^{fp}\}_{\infty,M}. \tag{24}$$

Numerical experiments and analysis (Pope, 1995; Xu and Pope, 1999) validate the following model for the bias error:

$$B_F = \frac{b_F(M)}{N_{pc}}, \tag{25}$$

where the bias coefficient b_F indicates the magnitude of bias for a given N_{pc}. Note that the bias coefficient b_F is assumed to be a function of the grid size through M. It is important to note that MIS can reduce statistical error, but not the bias error. The only way to reduce bias error is to increase N_{pc}.

Finally, the discretization error is identified as the remaining deterministic error in ϵ_F, such that

$$S_F \equiv \{\mathbf{F}_m^{\mathrm{fp}}\}_{\infty,M} - \langle \mathbf{F}_m^{\mathrm{fp}} \rangle. \tag{26}$$

The discretization error for most finite-difference/finite-volume CFD schemes with power-law truncation error dependence can be modeled as

$$S_F = \frac{a_F}{M^p}, \tag{27}$$

where a_F is the discretization error coefficient and the exponent p depends on the order of convergence of the numerical scheme. In a time-dependent problem, the discretization error will also include a contribution from the temporal discretization error, and all the aforementioned error definitions will be parametrized by the time step Δt, in addition to N_{pc} and M.

4. Results

4.1. Test 1: Baseline test case

The baseline test case with transcendental mean fluid velocity field, and uniformly distributed particles with delta-function particle velocity distribution was defined in Section 2. This test is simulated with periodic boundary conditions on the unit cube for each numerical scheme. In all the results presented, the estimate and as well as analytical values for the interphase momentum transfer term are normalized by the maximum analytical value $\langle \mathbf{F}^{\mathrm{fp}} \rangle_{\max}$ in the domain. Therefore, all the individual error contributions are also normalized.

4.1.1. Forward interpolation error

Fig. 4 shows the forward interpolation error defined by Eq. (19) as a function of cell size $h = (\Delta x \Delta y)^{1/2}$. In the results shown, the number of particles per cell $N_{\mathrm{pc}} = 100$, and the grid varies from $21 \times 21 \times 4$ nodes to $61 \times 61 \times 4$ nodes. The figure shows that the fourth-order LPI-4 scheme is the most accurate of all the schemes, and it also has the highest rate of convergence. The least accurate scheme is PCA, and the reason is because this approximation scheme does not exactly recover nodal values, unlike the other three schemes that are true interpolation schemes. The PCA results converge with second-order accuracy, as expected. Since TSE uses linear basis functions for forward interpolation (see Appendix A), its accuracy and convergence are identical to that of LPI-2. The data show that the numerical schemes follow their theoretical rates of convergence, which is four for LPI-4, and two for LPI-2, TSE, and PCA (Monaghan, 1992).

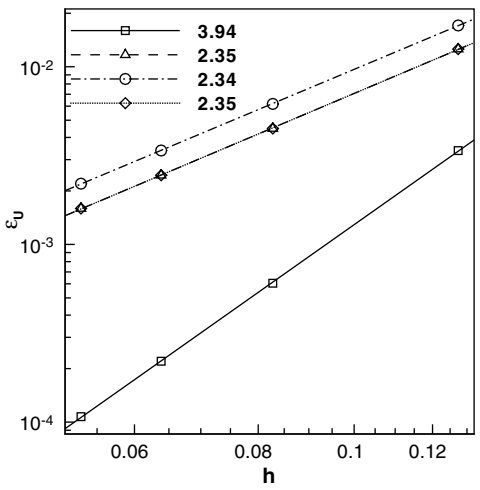

Fig. 4. Convergence of forward interpolation error ϵ_U with grid spacing h. □, LPI-4; △, LPI-2; ○, PCA, ◇, TSE. The values in the legend are the slope of linear least-squares fit to the data. These are close to the order of the schemes.

4.1.2. Statistical error

Although Eq. (22) provides a formal definition of the statistical error, actually computing the statistical error requires a numerical estimate of $\langle\{\mathbf{F}_m^{\mathrm{fp}}\}_{N_{\mathrm{pc}},M}\rangle$. We estimate $\langle\{\mathbf{F}_m^{\mathrm{fp}}\}_{N_{\mathrm{pc}},M}\rangle$ by performing $\mathscr{M}$ multiple independent realizations, each with the same N_{pc} and on the same grid M but initialized with different random seeds, and taking the arithmetic mean of the MIS. An estimate of the statistical error $\widehat{\Sigma}_F$ can now be obtained by replacing $\langle\{\mathbf{F}_m^{\mathrm{fp}}\}_{N_{\mathrm{pc}},M}\rangle$ in Eq. (22) with its MIS estimate $\langle\{\mathbf{F}_m^{\mathrm{fp}}\}_{N_{\mathrm{pc}},M}\rangle_{\mathscr{M}}$, to get

$$\widehat{\Sigma}_F \equiv \{\mathbf{F}_m^{\mathrm{fp}}\}_{N_{\mathrm{pc}},M} - \langle\{\mathbf{F}_m^{\mathrm{fp}}\}_{N_{\mathrm{pc}},M}\rangle_{\mathscr{M}}. \tag{28}$$

The scaling of this estimate for the statistical error with $\mathscr{M}$ is revealed by defining $\Sigma_{F,\mathscr{M}} \equiv \langle\{\mathbf{F}_m^{\mathrm{fp}}\}_{N_{\mathrm{pc}},M}\rangle_{\mathscr{M}} - \langle\{\mathbf{F}_m^{\mathrm{fp}}\}_{N_{\mathrm{pc}},M}\rangle$, and rewriting $\widehat{\Sigma}_F$ as

$$\widehat{\Sigma}_F = \Sigma_F - \Sigma_{F,\mathscr{M}} = \frac{c_F\theta}{\sqrt{N_{\mathrm{pc}}}} - \frac{c_F\xi}{\sqrt{(\mathscr{M}N_{\mathrm{pc}})}}, \tag{29}$$

where θ and ξ are independent standardized normal random variables. (See Appendix B for details.) The scaling shows that $\langle\{\mathbf{F}_m^{\mathrm{fp}}\}_{N_{\mathrm{pc}},M}\rangle_{\mathscr{M}} \to \langle\{\mathbf{F}_m^{\mathrm{fp}}\}_{N_{\mathrm{pc}},M}\rangle$ as $\mathscr{M}^{-1/2}$ for sufficiently large $\mathscr{M}$, and this is true for any $N_{\mathrm{pc}} > 1$. This $\mathscr{M}^{-1/2}$ scaling is verified by the plot in Fig. 5a of $\mathrm{rms}(\widehat{\Sigma}_F)$ as a function of $\mathscr{M}$ at $(x = 0.5, y = 0.5)$ for a fixed number of particles $N_{\mathrm{pc}} = 100$ and a $21 \times 21 \times 4$ grid. The slopes of the least-squares line fits to the data from all schemes are close to -0.5. This plot also tells us that using MIS we can reduce the statistical error $\Sigma_{F,\mathscr{M}}$, which scales as $(\mathscr{M}N_{\mathrm{pc}})^{-1/2}$, to negligible levels compared to the other error contributions.

We now verify the dependence of $\Sigma_{F,\mathscr{M}}$ on N_{pc} that is predicted by Eq. (29). Fig. 5b shows the variation of $\mathrm{rms}(\widehat{\Sigma}_F)$ with N_{pc} for a fixed number of realizations $\mathscr{M} = 100$ on a $21 \times 21 \times 4$ grid at a representative location $(x = 0.5, y = 0.5)$. The slopes of the least-squares line fits to the data are all close to -0.5, thus verifying the expected convergence of the statistical error as $N_{\mathrm{pc}}^{-1/2}$ that is predicted by Eq. (29). For the baseline case of zero particle velocity variance there is little difference in the statistical error incurred by various schemes. Even with just 10 particles per cell the statistical error is $\mathrm{O}(10^{-4})$.

When computing the contributions from bias error and deterministic error to the total error using Eq. (21), the statistical error will need to be negligibly small in comparison. From Eq. (28) we can infer that if the product $N_{\mathrm{pc}}\mathscr{M}$ is sufficiently large, then the statistical error can be made arbitrarily small. In this case the estimate for average interphase momentum transfer term $\langle\{\mathbf{F}_m^{\mathrm{fp}}\}_{N_{\mathrm{pc}},M}\rangle_{\mathscr{M}}$ will have a very small and spatially uniform statistical error for different values of N_{pc}. The results for deterministic and bias error presented in the following subsections correspond to $N_{\mathrm{pc}}\mathscr{M} = 60,000$, which ensures very low statistical error.

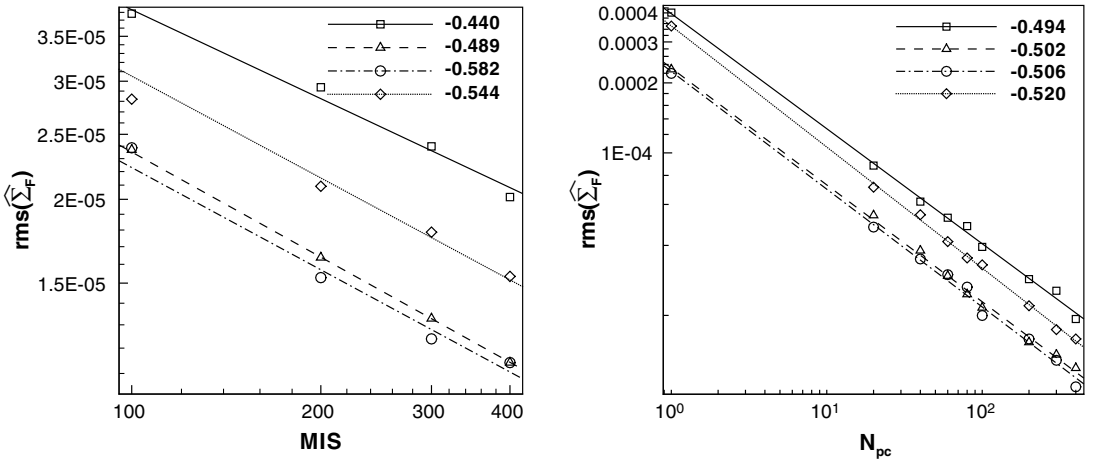

(a) Convergence with MIS ($N_{pc} = 100$). (b) Convergence with N_{pc} ($\mathcal{M} = 100$).

Fig. 5. Convergence of statistical error $\mathrm{rms}(\widehat{\Sigma}_F)$ with (a) number of multiple independent simulations $\mathscr{M}$, and (b) number of particles per cell N_{pc}, at $(x = 0.5, y = 0.5)$ for Test 1 with zero particle velocity variance ($V_1^* \overset{D}{=} \mathcal{N}[1.0, 0.0]$). □, LPI-4; △, LPI-2; ○, PCA, ◇, TSE. The values in the legend are the slope of linear least-squares fit to the data.

4.1.3. Deterministic error

The total deterministic error D_F is estimated by $\hat{D}_F$ using an ensemble-averaged estimator at finite N_{pc} and the analytical solution:

$$\widehat{D}_F = \left| \langle \{\mathbf{F}_m^{\mathrm{fp}}\}_{N_{\mathrm{pc}},M} \rangle_{\mathscr{M}} - \langle \mathbf{F}_m^{\mathrm{fp}} \rangle \right|. \tag{30}$$

The contour plot of deterministic error estimated by Eq. (30) is shown in Fig. 6 for a $21 \times 21 \times 4$ grid with $N_{\mathrm{pc}} = 400$ using $\mathscr{M} = 150$ independent realizations ($N_{\mathrm{pc}}\mathscr{M} = 60,000$). Of the four schemes, LPI-4 incurs the least total deterministic error and the magnitude of error incurred by the other three schemes is comparable. The figure also shows that the location of the maximum deterministic error is not the same for all schemes. Therefore, a comparison of deterministic error incurred by the different schemes at a fixed location can be misleading.

4.1.4. Bias error

Bias error, which is defined by Eq. (24) in Section 3.1, is that part of the deterministic error resulting from a finite number of particles. Similar to the estimation of expected values that arise in the statistical error, the quantity $\langle \{\mathbf{F}_m^{\mathrm{fp}}\}_{N_{\mathrm{pc}},M} \rangle$ in the bias error is approximated by an ensembled-averaged estimate $\langle \{\mathbf{F}_m^{\mathrm{fp}}\}_{N_{\mathrm{pc}},M} \rangle_{\mathscr{M}}$. Therefore, the approximate expression for bias error $\widehat{B}_F$ is

$$\widehat{B}_F = \langle \{\mathbf{F}_m^{\mathrm{fp}}\}_{N_{\mathrm{pc}},M} \rangle_{\mathscr{M}} - \{\mathbf{F}_m^{\mathrm{fp}}\}_{\infty,M} = \frac{b_F(M)}{N_{\mathrm{pc}}}. \tag{31}$$

In order to calculate the bias error based on this definition, it is necessary to compute $\{\mathbf{F}_m^{\mathrm{fp}}\}_{N_{\mathrm{pc}},M}$ at $N_{\mathrm{pc}} = \infty$ which is impractical and computationally prohibitive. However, noting that the magnitude of the bias coeffi-

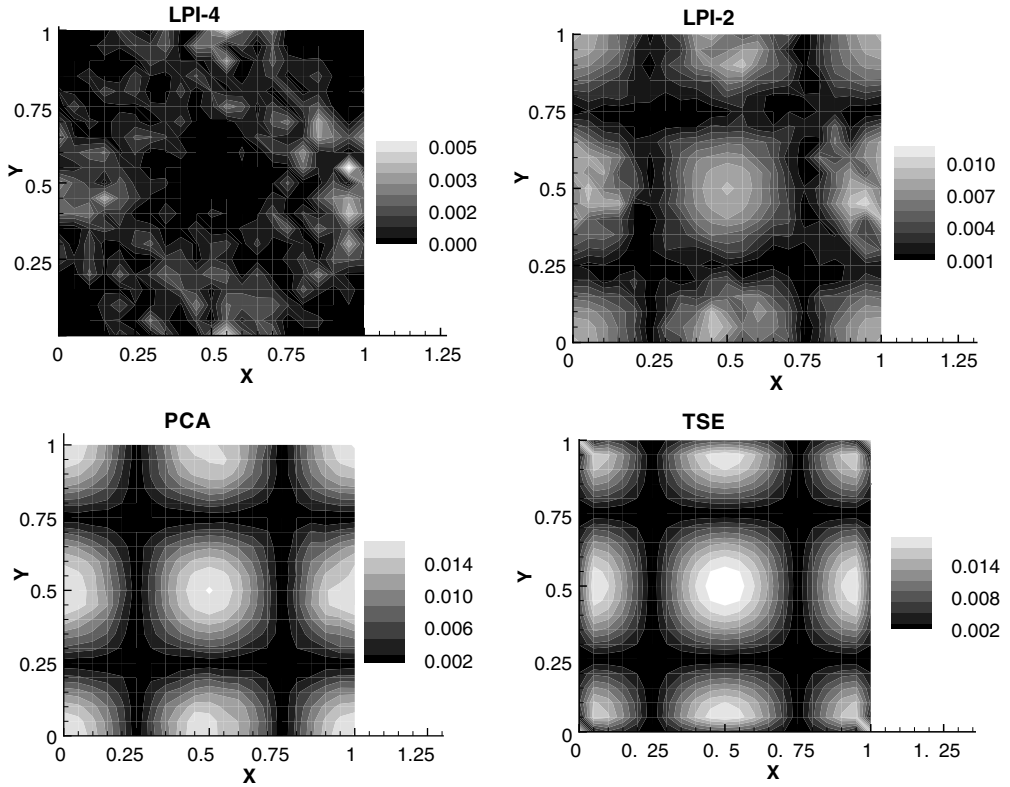

Fig. 6. Contour plot of total deterministic error for Test 1 on a $21 \times 21 \times 4$ grid with $N_{\mathrm{pc}} = 400$ and $N_{\mathrm{pc}}\mathscr{M} = 60,000$. The fourth-order LPI-4 scheme exhibits least error. All schemes show considerable spatial variation with an order of magnitude difference in the total deterministic error across the domain.

cient b_F is a function of only the grid size M, we can use two evaluations of $\langle\{\mathbf{F}_m^{\mathrm{fp}}\}_{N_{\mathrm{pc}},M}\rangle_{\mathscr{M}}$ at $N_{\mathrm{pc}} = N_{\mathrm{pc}}^{(1)}$ and $N_{\mathrm{pc}}^{(2)}$ to calculate b_F as follows:

$$b_F(M) = \frac{N_{\mathrm{pc}}^{(1)} N_{\mathrm{pc}}^{(2)}}{N_{\mathrm{pc}}^{(2)} - N_{\mathrm{pc}}^{(1)}} \left(\langle\{\mathbf{F}_m^{\mathrm{fp}}\}_{N_{\mathrm{pc}}^{(1)},M}\rangle_{\mathscr{M}} - \langle\{\mathbf{F}_m^{\mathrm{fp}}\}_{N_{\mathrm{pc}}^{(2)},M}\rangle_{\mathscr{M}} \right). \tag{32}$$

If more than two values of N_{pc} are used, the slope obtained from a linear least-squares fit to the data yields the bias coefficient b_F.

Although there is considerable spatial variation of the bias error, the variation of $\langle\{\mathbf{F}_m^{\mathrm{fp}}\}_{N_{\mathrm{pc}},M}\rangle_{\mathscr{M}}$ with N_{pc}^{-1} is shown in Fig. 7 at the same representative location $(x = 0.5, y = 0, 5)$ where the statistical error scaling was shown. From the figure, the linear behavior of bias with N_{pc}^{-1} is apparent. Since the total deterministic error exhibits different spatial distribution for each scheme, a contour plot of the bias coefficient b_F is more informative. The bias coefficient is calculated using Eq. (32), and Fig. 8 shows that TSE is the least biased estimator (by two orders of magnitude compared to the other schemes considered) followed by PCA, LPI-2, and LPI-4.

4.1.5. Discretization error

Discretization error defined by Eq. (26) depends only on the spatial resolution, or grid size, h. A smaller value of h (more grid points) for a given N_{pc} will yield a more resolved mean field, and hence a lower discretization error.

Similar to observations made for bias error, if the discretization error is estimated based on its definition (cf. Eq. (26)), then one needs to calculate $\{\mathbf{F}_m^{\mathrm{fp}}\}_{\infty,M}$ which is impractical. Therefore, we calculate S_F by forming an approximate estimate for $\{\mathbf{F}_m^{\mathrm{fp}}\}_{\infty,M}$ denoted by $\{\mathbf{F}_m^{\mathrm{fp}}\}_e$. For a fixed grid size M with known bias coefficient b_F (see Eq. (31)), the estimate of $\{\mathbf{F}_m^{\mathrm{fp}}\}_{N_{\mathrm{pc}},M}$ in the limit of N_{pc} going to infinity is obtained by Richardson extrapolation (Xu and Pope, 1999) of $\langle\{\mathbf{F}_m^{\mathrm{fp}}\}_{N_{\mathrm{pc}},M}\rangle_{\mathscr{M}}$ at two or more values of N_{pc}. The expression for $\{\mathbf{F}_m^{\mathrm{fp}}\}_e$ is

$$\{\mathbf{F}_m^{\mathrm{fp}}\}_e = \frac{\sum_{i=1}^{\mathscr{N}} \langle\{\mathbf{F}_m^{\mathrm{fp}}\}_{N_{\mathrm{pc}}^{(i)},M}\rangle_{\mathscr{M}} - b_F \sum_{i=1}^{\mathscr{N}} (N_{\mathrm{pc}}^{(i)})^{-1}}{\mathscr{N}} \cong \{\mathbf{F}_m^{\mathrm{fp}}\}_{\infty,M}, \tag{33}$$

where $\mathscr{N}$ is the number of N_{pc} values for which the ensemble-averaged estimates are formed for each grid size M. In the estimation of bias coefficient, the effect of statistical fluctuations is minimized by choosing $N_{\mathrm{pc}}\mathscr{M} = 60,000$. Furthermore, in the above expression for estimating $\{\mathbf{F}_m^{\mathrm{fp}}\}_e$, the effect of bias is also removed

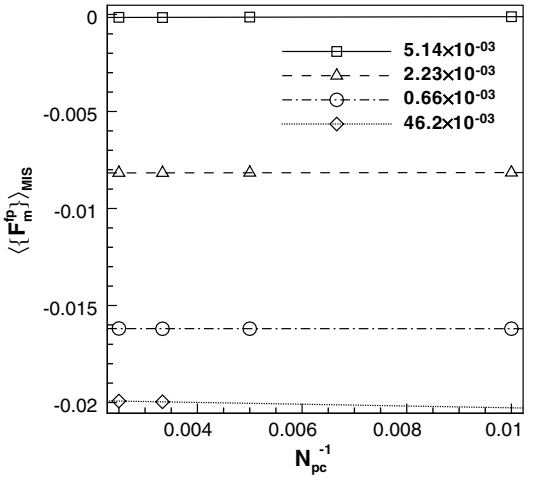

Fig. 7. Estimation of bias coefficient b_F from plot of $\langle\{\mathbf{F}_m^{\mathrm{fp}}\}_{N_{\mathrm{pc}},M}\rangle_{\mathscr{M}}$ as a function of N_{pc}^{-1} for $N_{\mathrm{pc}}\mathscr{M} = 60,000$ at $(x = 0.5, y = 0, 5)$. □, LPI-4; △, LPI-2; ○, PCA, ◇, TSE. The slope of the linear least-squares fit, which is also equal to the bias coefficient, is indicated in the legend.

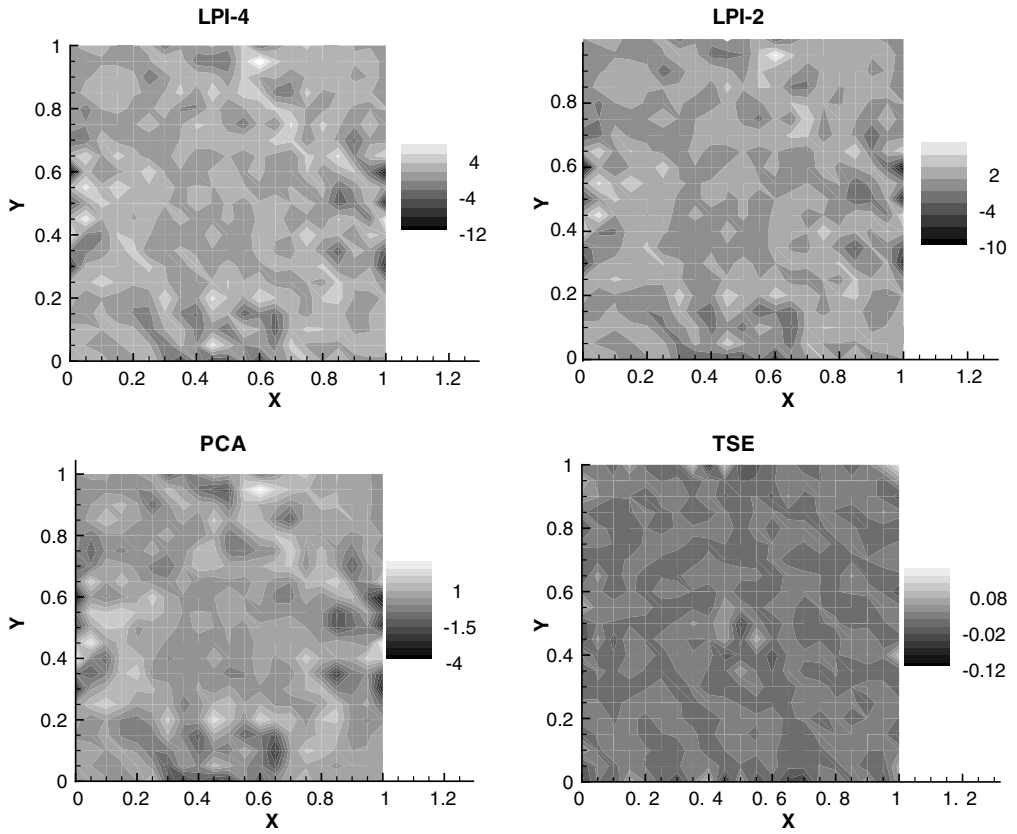

Fig. 8. Contour plot of the bias coefficient b_F for Test 1 on a $21 \times 21 \times 4$ grid ($N_{\text{pc}} \mathscr{M} = 60,000$). TSE incurs the least bias error with a bias coefficient that is two orders of magnitude lower than the other schemes.

from the numerical estimate. The effects of both statistical fluctuations and bias error are minimized in the estimate of $\{\mathbf{F}_m^{\text{fp}}\}_e$; thus, $\{\mathbf{F}_m^{\text{fp}}\}_e$ is a good approximate estimate for $\{\mathbf{F}_m^{\text{fp}}\}_{\infty,M}$.

Figs. 9a and b show the convergence of spatial discretization error $S_F = |\{\mathbf{F}_m^{\text{fp}}\}_e - \langle \mathbf{F}_m^{\text{fp}} \rangle|$ with cell size $h = (\Delta x \Delta y)^{1/2}$ at two representative (x, y) locations $(0.5, 0.5)$ and $(0.6, 0.2)$, respectively. Fig. 9a shows that at the $(0.5, 0.5)$ location, LPI-4 incurs the least discretization error and has the highest rate of convergence; followed by LPI-2, PCA, and TSE. The convergence rates are once again very close to the theoretical values and show trends similar to those observed for forward interpolation error in Section 4.1.1. At the $(0.6, 0.2)$ location, however, Fig. 9b shows that the convergence rate of all schemes have changed considerably. LPI-4 now has the lowest rate of convergence. PCA, on the other hand, is the fastest converging scheme followed by TSE and LPI-2.

Since the rate of convergence of spatial discretization error (Fig. 9) exhibits strong spatial non-uniformity for each scheme, a global discretization error

$$\widehat{S}_F = \frac{1}{M} \sqrt{\sum_{m=1}^{M} \left(\{\mathbf{F}_m^{\text{fp}}\}_e - \langle \mathbf{F}_m^{\text{fp}} \rangle \right)^2} \tag{34}$$

is defined using the standard rms technique given by Eq. (34), with $M = M_x \times M_y \times M_z$ being the total number of grid nodes. Fig. 10 shows the convergence of global discretization error $\widehat{S}_F$ with grid spacing h. The figure reveals a deficiency in LPI-4, which is no longer the fastest converging scheme. This sharp fall in the convergence rate of global discretization error incurred by LPI-4 can be explained as a result of strong spatial non-uniformity of local convergence rates observed in Fig. 9. On a coarse grid (high value of h), LPI-4 is the most

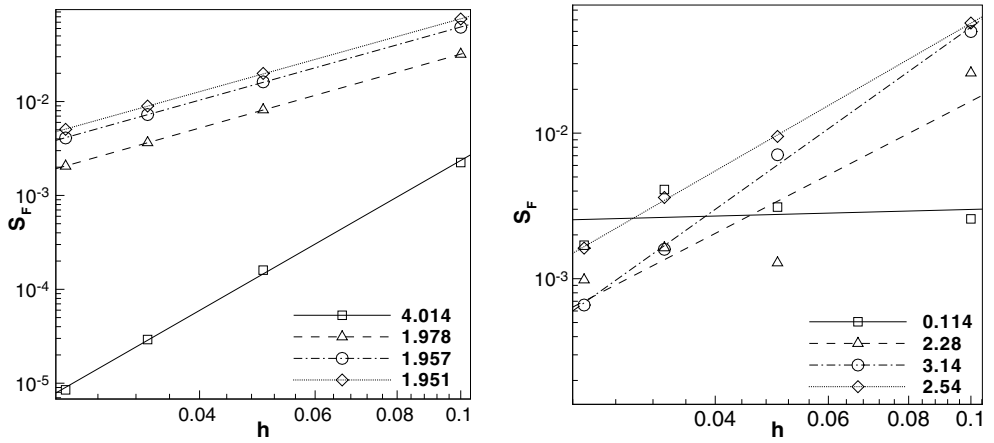

(a) Convergence of S_F at $(0.5, 0, 5)$. (b) Convergence of S_F at $(0.6, 0.2)$.

Fig. 9. Convergence of spatial discretization error $S_F = \left|\{\mathbf{F}_m^{\text{fp}}\}_e - \langle \mathbf{F}_m^{\text{fp}} \rangle\right|$ with grid spacing h at different spatial locations to illustrate the strong spatial non-uniformity in convergence characteristics of the schemes: (a) convergence of S_F with h at $(x = 0.5, y = 0.5)$ for Test 1, (b) convergence of S_F with h at $(x = 0.6, y = 0.2)$ for Test 1. □, LPI-4; △, LPI-2; ○, PCA, ◇, TSE. The slope of the linear least-squares fit is indicated in the legend.

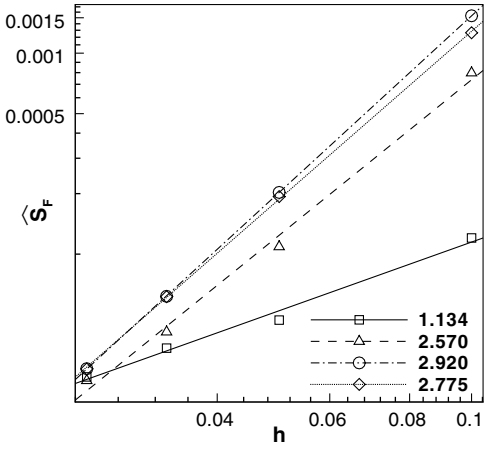

Fig. 10. Convergence of global discretization error $\widehat{S}_F$ with grid spacing h for Test 1. □, LPI-4; △, LPI-2; ○, PCA, ◇, TSE. The slope of the linear least-squares fit is indicated in the legend. Note the dramatic difference in convergence rates that deviate considerably from the order of the schemes, in contrast to Fig. 4.

accurate estimator but it is least accurate on fine grids (at lower h) due to the slow rate of convergence of its global discretization error. PCA exhibits the highest rate of convergence of global discretization error, followed by TSE, LPI-2, and LPI-4.

Our results for this test case of zero particle velocity variance show that the statistical error for all schemes is of the same order of magnitude. However, based on the magnitude of bias error, and the rate of convergence of global discretization error, TSE and PCA stand out as the preferred methods for estimating the mean interphase momentum transfer term.

4.2. Test 2: Effect of non-zero particle velocity variance

In this test we investigate the effect of non-zero particle velocity variance that is representative of many practical particle-laden flows. Non-zero particle velocity variance may arise as a result of turbulence. The only

change from the baseline test is the particle velocity distribution, which is now specified to be a normal with non-zero variance:

$$V_1^* \stackrel{D}{=} \mathcal{N}[\langle V_1 \rangle,\ \sigma^2_{V_1}] \equiv [1.0, 0.3]. \tag{35}$$

Since the particle velocity distribution now has a finite variance, it is expected that the statistical error in estimating the mean interphase momentum transfer term will be larger than that incurred in the baseline test case with zero variance (cf. Fig. 5).

Fig. 11 shows the statistical error incurred by the various schemes for finite particle velocity variance, but with all other test conditions identical to those in Fig. 5. As expected, the statistical error shows an increase for all the schemes (by at least one order of magnitude), but the increase is not the same for all schemes. While in the baseline test with zero particle velocity variance the statistical error is $O(10^{-4})$ even with just 10 particles per cell for all the schemes (cf. Fig. 5b), Fig. 11b shows that for $\sigma^2_{V_1} = 0.3$ with 10 particles per cell the statistical error is at least an order of magnitude higher $O(10^{-3} - 10^{-2})$. If the particle velocity variance is not zero, Fig. 11b also shows that the LPI-4 and LPI-2 schemes incur statistical error that is an order of magnitude larger than that incurred by TSE or PCA. The difference in the statistical error incurred by the schemes persists even with increasing MIS, as shown in Fig. 11a.

The bias coefficient b_F contours for Test 2 exhibit similar spatial variation for all the schemes as seen in Test 1 (see Fig. 8), and are hence not presented here. However, an important effect of non-zero particle velocity variance is to significantly increase the bias coefficient values for TSE (min/max: $-2/0.5$), whereas those of LPI-4 (min/max: $-10/6$), LPI-2 (min/max: $-8/4$), and PCA (min/max: $-3/3$) remain at levels similar to that seen in Test 1. Nevertheless, even for this test TSE incurs the least bias error of all the schemes considered.

Fig. 12 shows the variation of global discretization error $\hat{S}_F$ with h, which when compared to the previous case of zero variance (Fig. 10) shows that the magnitude of global discretization error and as well as its rate of convergence remain nearly the same. This observation is not surprising because the only difference between the two test cases is in the particle velocity distribution, which should not affect the discretization error.

Both TSE and PCA outperform LPI-4 and LPI-2 in terms of statistical error and incur relatively low bias error. Also, the rate of convergence of global discretization error for TSE and PCA is nearly twice that of LPI-4. The results of this test reaffirm the conclusions of Test 1 that both TSE and PCA are the best schemes to estimate the mean interphase momentum transfer term.

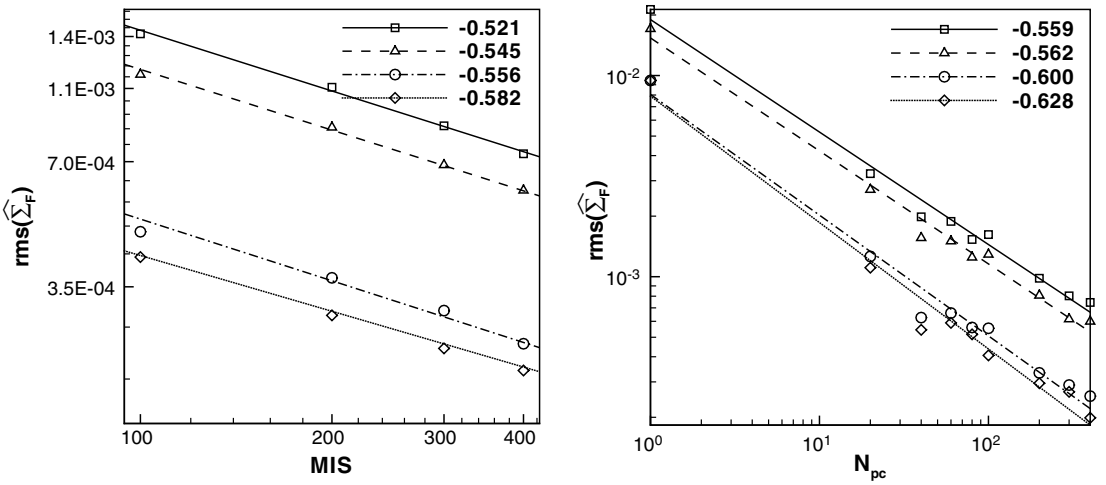

(a) Convergence with $\mathcal{M}$ ($N_{pc} = 100$). (b) Convergence with N_{pc} ($\mathcal{M} = 100$).

Fig. 11. Convergence of statistical error rms($\widehat{\Sigma}_F$) with (a) number of multiple independent simulations $\mathcal{M}$, and (b) number of particles per cell N_{pc}, at ($x = 0.5, y = 0.5$) for Test 2 with non-zero particle velocity variance ($V_1^* \stackrel{D}{=} \mathcal{N}[1.0, 0.3]$). □, LPI-4; △, LPI-2; ○, PCA, ◇, TSE. The slope of the linear least-squares fit is indicated in the legend.

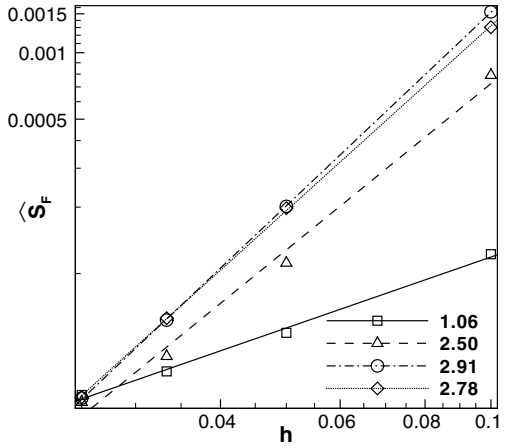

Fig. 12. Convergence of global discretization error $\hat{S}_F$ with grid spacing h for Test 2. □, LPI-4; △, LPI-2; ○, PCA, ◇, TSE. The slope of the linear least-squares fit is indicated in the legend. Comparison with Fig. 10 reveals that the effect of non-zero particle velocity variance on the magnitude and convergence rate of the global discretization error is minimal.

4.3. Test 3: Variation of particle position distribution

In our numerical tests thus far we have chosen the particles to be uniformly distributed in physical space. However, in realistic particle-laden flows the particles will not be uniformly distributed in general. In this test, the fluid velocity field and particle velocity distribution are retained as in Test 2 (finite variance). In order to ascertain the effect of non-uniform particle distribution, the particle number density field is specified to be

$$n(x,y) = n_o \exp\left(-\frac{(x-\mathscr{L}_x/2)^2 + (y-\mathscr{L}_y/2)^2}{\mathscr{L}_x^2/16 + \mathscr{L}_y^2/16}\right), \tag{36}$$

where n_o is a constant so chosen such that there are a finite number of particles near the boundary cells. Fig. 13a shows the contour plot for $n(x,y)/n_o$. Using the particle position pdf $f_{\mathbf{X}} = n(\mathbf{x})/\langle N_p \rangle$ implied by the number density in Eq. (36), the analytical expression for normalized mean interphase momentum transfer term is obtained from Eq. (16). Fig. 13b shows the resulting normalized mean interphase momentum transfer

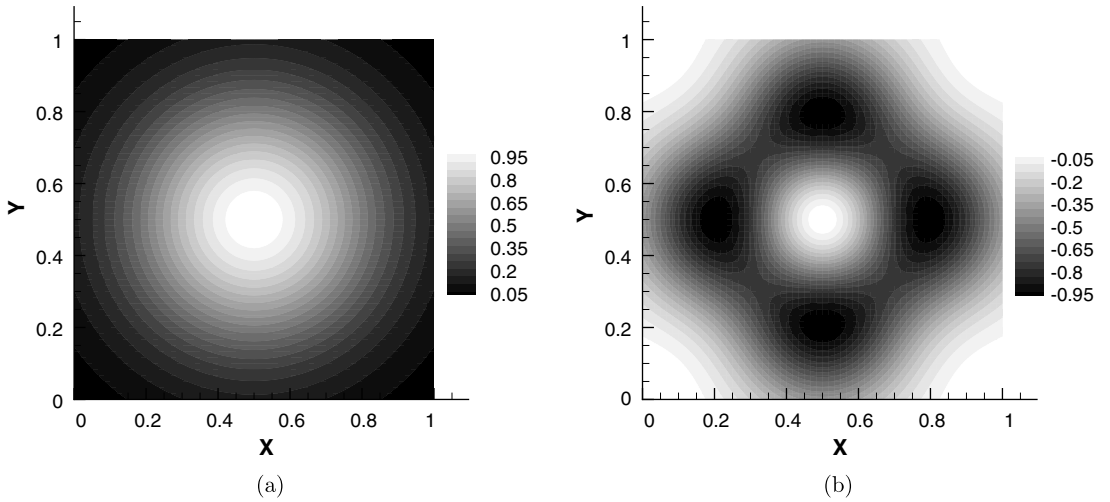

Fig. 13. Test 3 with non-uniform particle position distribution: (a) Contour plot of the scaled number density $n(x,y)/n_o$. (b) Contour plot of the scaled analytical mean interphase momentum transfer term $\langle F_x^{\mathrm{fp}} \rangle / \langle F_x^{\mathrm{fp}} \rangle_{\max}$.

term. In this inhomogeneous test case no attempt is made to decompose the various numerical errors, but only the error resulting from the averaged estimate obtained from multiple realizations along with the 95% confidence intervals are presented. The 95% confidence interval (Xu and Pope, 1999) for the estimation of interphase momentum transfer term is estimated as

$$\delta = 1.69\left[\frac{1}{\mathscr{M}-1}\sum_{i=1}^{\mathscr{M}}\left(\{\mathbf{F}_m^{\mathrm{fp}}\}_{N_{\mathrm{pc}},M}^{(i)} - \langle\{\mathbf{F}_m^{\mathrm{fp}}\}_{N_{\mathrm{pc}},M}\rangle_{\mathscr{M}}\right)^2\right]^{1/2}. \tag{37}$$

The test is carried out on a $61\times61\times4$ grid and 200 independent but identical simulations are performed in order to calculate the 95% confidence intervals. In Fig. 14a, the symbols indicate the ensemble-averaged mean interphase momentum transfer term $\langle\{\mathbf{F}_m^{\mathrm{fp}}\}_{N_{\mathrm{pc}},M}\rangle_{\mathscr{M}}$ obtained using LPI-4 and LPI-2. The scale for the symbols is on the left vertical axis. The height of the error bars indicate the 95% confidence intervals on the ensemble average, and in order to distinguish between the two cases the error bars with the longer cross-bar indicate LPI-4. In the same figure, the lines represent $|\langle\mathbf{F}_m^{\mathrm{fp}}\rangle - \langle\{\mathbf{F}_m^{\mathrm{fp}}\}_{N_{\mathrm{pc}},M}\rangle_{\mathscr{M}}|$, the error between the ensemble-averaged and analytical mean interphase momentum transfer term. The scale for the error is on the right vertical axis. Since the number density variation in x and y is identical, the ensemble-averaged mean interphase momentum transfer term and error are reported along x, for $y = z = 0.5$. Fig. 14b shows results for the same test as Fig. 14a, but for the PCA and TSE schemes. The longer cross-bars on the 95% confidence intervals correspond to PCA.

For all the schemes considered, the size of the confidence interval shows an increase in the regions of low number density. This increase is maximum for LPI-4 followed by LPI-2, PCA, and TSE. The error shows the same trend in the regions of low number density. This test shows the advantage of using TSE and PCA over LPI-4 and LPI-2 for particle-laden systems with non-uniform number density.

4.4. Test 4: Variation of fluid velocity field

Depending on the type of simulation (CFD, LES or DNS), the spectral content of the fluid velocity field will be different. In this test, the fluid velocity field is chosen to be a sinusoidal field given by Eq. (38) and its wavelength is varied by increasing f_o from a minimum value of 1 to a maximum value of 25. This test reveals the accuracy of mean interphase momentum transfer term estimation with variation in the fluid velocity spectrum of the velocity field

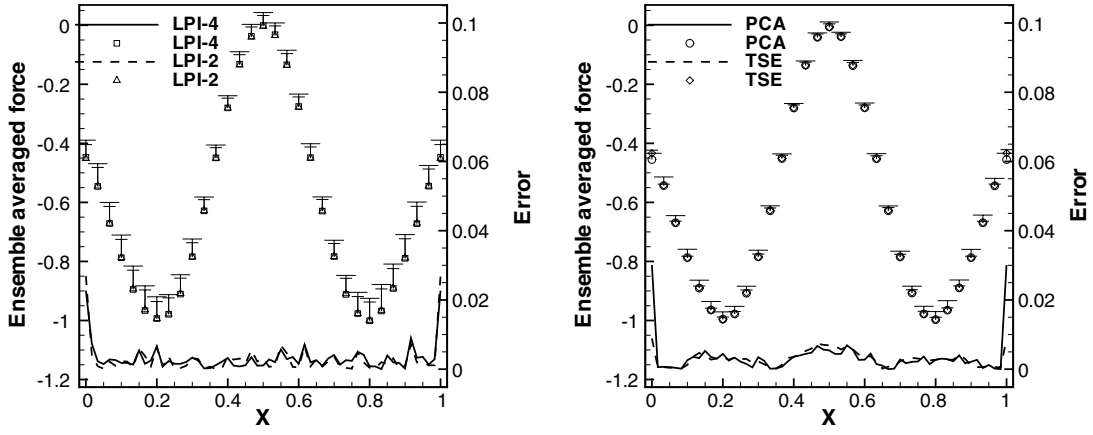

(a) LPI-4 and LPI-2. (b) PCA and TSE.

Fig. 14. Ensemble-averaged mean interphase momentum transfer term for Test 3 with confidence intervals, and its error with respect to analytical value. In both panels the symbols indicate $\langle\{\mathbf{F}_m^{\mathrm{fp}}\}_{N_{\mathrm{pc}},M}\rangle_{\mathscr{M}}$ (scale on left vertical axis) as a function of x at $y = z = 0.5$. Error bars denote 95% confidence intervals above and below the mean value, but are shown only above for clarity. The error bars for the two schemes in each panel are distinguished by the length of the cross-bars, with (a) LPI-4 (long), LPI-2 (short), and (b) PCA (long), TSE (short). Lines in both panels indicate the error $\left|\langle\mathbf{F}_m^{\mathrm{fp}}\rangle - \langle\{\mathbf{F}_m^{\mathrm{fp}}\}_{N_{\mathrm{pc}},M}\rangle_{\mathscr{M}}\right|$ whose scale is given on the right vertical axis.

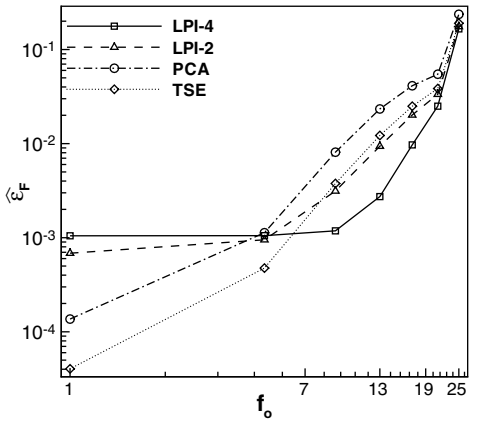

Fig. 15. Ensemble-averaged summed mean square error $\hat{\epsilon}_F$ as a function of f_o, the frequency of the transcendental velocity field.

$$U_1^{\mathrm{f}}(x,y) = \cos\left(\frac{2\pi f_o x}{\mathscr{L}_x}\right)\cos\left(\frac{2\pi f_o y}{\mathscr{L}_y}\right). \tag{38}$$

The ensemble-averaged summed mean square of the total error, denoted by $\hat{\epsilon}_F$, and given by the following expression

$$\hat{\epsilon}_F = \frac{1}{\mathscr{M}}\sum_{i=1}^{\mathscr{M}}\frac{\sum_{m=1}^{M^3}\left(\{\mathbf{F}_m^{\mathrm{fp}}\}^i - \langle\mathbf{F}_m^{\mathrm{fp}}\rangle\right)^2}{M^3} \tag{39}$$

is calculated for different values of f_o.

Particles are uniformly distributed in physical space and the particle velocity field of Test 2 (finite variance) is retained here. The number of computational particles per cell N_{pc} is 100 and number of realizations $\mathscr{M} = 150$. The test is performed on a $51\times51\times4$ grid.

Fig. 15 shows the variation of $\hat{\epsilon}_F$ versus f_o and it can be observed that at low wavenumbers TSE and PCA outperform LPI-4 and LPI-2 by an order of magnitude, at intermediate wavenumbers LPI-4 and LPI-2 become more accurate than PCA and TSE, and at the highest wavenumber, all the schemes are rather inaccurate and have approximately the same error magnitude. The reduction in accuracy for PCA and TSE from low to intermediate wavenumbers compared to LPI-4 and LPI-2 is attributed to the smoothing property of cubic splines and linear least-squares, respectively. Therefore, for LES and DNS simulations, PCA and TSE will require higher grid resolution to yield the same accuracy as LPI-4 or LPI-2.

5. Comparison with representative LE numerical parameters

In this study we have performed calculations with very high numerical resolution. The number of particles per cell in our tests typically ranges from 100 to 400. In addition, the number of independent realizations simulated for each test also varies from 100 to 400. However, in most particle-laden simulations of two-way coupled dispersed two-phase flows using LE approach, the number of particles per cell is usually one or even two orders of magnitude lower than the values we have used for our tests, and typically only one realization is simulated. Typical values for the nominal number of particles per cell[5] in 3-D LE simulations range from 0.0156 to 0.125 in (Sundaram and Collins, 1999) to exactly 1 in (Boivin et al., 1998). In 2-D calculations higher N_{pc}^n values have been used: 3–30 in Narayanan et al. (2002) and 16 to 500 in Lakehal and Narayanan (2003). In all but one of these studies (Lakehal and Narayanan, 2003), only one realization is simulated. The contour plot of absolute total error $\epsilon_F = \left|\{F_{x,m}^{\mathrm{fp}}\}_{N_{\mathrm{pc}},M} - \langle F_{x,m}^{\mathrm{fp}}\rangle\right|$ incurred in the calculation of mean interphase momentum transfer term for Test 2 on a $61\times61\times4$ grid with $N_{\mathrm{pc}} = 5$ and $\mathscr{M} = 1$ is shown by Fig. 16. The figure

[5] The nominal number of particles per cell N_{pc}^n is defined as the ratio of total number of particles to total number of grid cells.

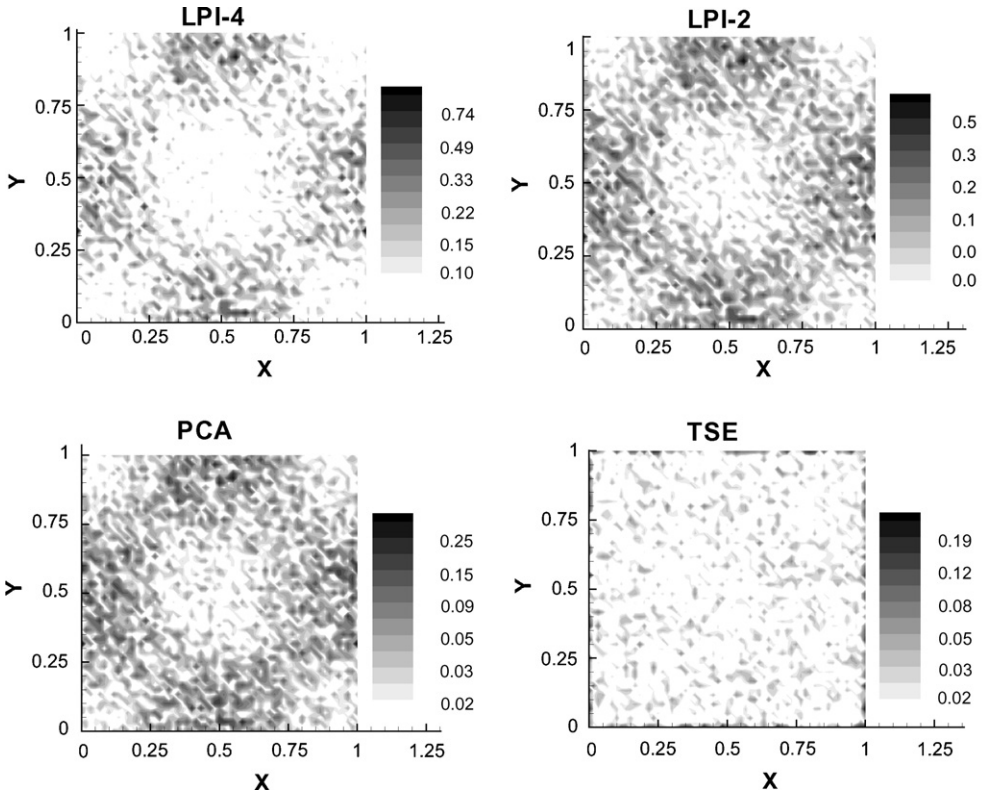

Fig. 16. Contour plot of absolute total error $\epsilon_F = |\{F^{\mathrm{fp}}_{x,m}\}_{N_{\mathrm{pc}},M} - \langle F^{\mathrm{fp}}_{x,m}\rangle|$ for Test 2 with representative LE numerical parameters—a single realization $\mathscr{M} = 1$ with $N_{\mathrm{pc}} = 5$ particles per cell on a $61 \times 61 \times 4$ grid—to demonstrate the unacceptably large errors incurred by schemes such as LPI-4 and LPI-2.

clearly reveals that while all the schemes are unable to provide estimates within 10% error using 5 particles per cell with only one realization, TSE comes closest with a maximum error of only 20%. LPI-4 gives errors as high as 80%. As noted in the introduction, these large numerical errors directly impact the physical insight that is provided by LE simulations. However, it is important to bear in mind that there are other numerical approximations in the fluid flow solver (artificial viscosity and pressure correction) that can mitigate these errors.

6. Conclusions

Comprehensive testing of four numerical schemes used to estimate mean interphase transfer terms in LE simulations for a novel test problem that admits an analytical solution enables characterization of numerical convergence, as well as accuracy. For estimation of the mean interphase momentum transfer term, all our four tests suggest the use of TSE and PCA, or even LPI-2, over LPI-4. TSE and PCA consistently give low statistical and bias errors and yield good estimates even in the regions of low number density. The only exception is when there is high spectral content in the fluid velocity field, where due to the smoothing nature of TSE and PCA, their estimates are less accurate than LPI-4 and LPI-2.

Testing with representative values for the numerical parameters found in typical LE simulations reveals that LPI-4 and LPI-2 incur unacceptably high error, whereas TSE yields the most accurate estimate of all the schemes. The tests validate an error model (cf. Eq. (21)) of the form

$$\epsilon_F = \frac{c_F\theta}{\sqrt{N_{\mathrm{pc}}}} + \frac{b_F(M)}{N_{\mathrm{pc}}} + \frac{a_F}{M^p}$$

that decomposes the error into statistical, bias and discretization components, and explicitly characterizes the error in terms of numerical parameters (grid size M and number of particles per cell N_{pc}). An approach to quantifying the values of the coefficients a_F, b_F, and c_F in the error model is demonstrated for the test problem. If efficient ways to quantify these coefficients are developed for general LE problems, then estimates for the numerical error can be obtained from this model. This can provide the required values of numerical parameters for a given error tolerance.

Our study reveals the need to carefully choose the appropriate numerical scheme for forward interpolation and backward estimation. Although LPI-4 is found to be the preferred scheme for forward interpolation, it results in relatively poor estimates for the mean interphase momentum transfer term. None of the schemes considered is optimal for both forward interpolation and backward estimation. This conclusion also implies that, for the schemes considered, the PIS requirement of Sundaram and Collins (1996)—which states that in order to ensure overall energy balance, the order of the interpolation scheme used in the forward interpolation should be the same as that used in the backward estimation—is at odds with numerical accuracy and convergence requirements.

Spatially non-uniform particle distribution results in poor estimates of mean interphase momentum transfer term in regions where there are fewer particles. If the number density of physical particles becomes zero locally, then TSE will encounter difficulties due to ill-conditioned matrices. One way to obtain good estimates even in regions of low physical particle number density is by introducing more computational particles in that region. In other words, if the number density of computational particles is maintained relatively uniform during the entire course of simulation, then the statistical error remains uniformly low over the entire domain. This needs to be addressed by computational particle number density control.

In order to obtain numerically converged results, it is imperative to simultaneously reduce the statistical and deterministic error components that result from backward estimation. The bias and statistical error components depend on the number of particles per cell. Therefore, numerical convergence cannot be achieved by grid refinement with a fixed total number of computational particles because the number of particles per cell keeps decreasing. This is because the bandwidth of most numerical schemes scales with the grid spacing.[6] Therefore, it is necessary to keep N_{pc} fixed in grid resolution studies of LE simulations so that statistical and bias error remain at the same level. While statistical error can be effectively reduced by multiple independent simulations, the same is not true for bias error, which scales as N_{pc}^{-1}. Time-evolving tests could show higher bias error due to feedback in the particle evolution equations. The only way to reduce bias error is to increase the number of computational particles per cell.

Another important consideration when choosing a numerical scheme for LE calculations is the computational cost involved, and the estimation of additional quantities that may be required. LPI-2 being a second-order scheme is the least expensive. PCA and LPI-4 involve the same number of operations while TSE is the computationally most expensive estimation scheme. However, if in addition to the mean interphase momentum transfer term, the estimation of its gradient is also required, then TSE becomes the favored scheme. This is because in TSE, once the interphase momentum transfer term has been calculated, no additional operations are required to compute the gradients. For LPI-4, LPI-2, and PCA, the estimation of gradient amounts to approximately doubling the computational cost that is required for calculating the mean interphase momentum transfer term.

Acknowledgement

SS and RG would like to thank David Schmidt for useful comments on this work.

Appendix A. Details of interpolation schemes

For the simplest PIC method (Crowe, 1982), the estimate for mean interphase momentum transfer term at grid node m enclosing volume V_m is given by

[6] An exception is TSE, which is a truly grid-free estimation method.

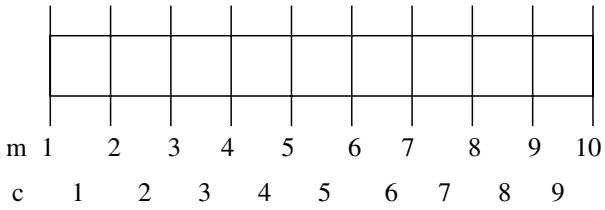

Fig. 17. 1-D grid showing grid nodes and cells.

$$\{\mathbf{F}_m^{\mathrm{fp}}\} = \frac{1}{V_m}\sum_{k=1}^{N_v}\mathbf{f}^k n_{\mathrm{p}}^k, \tag{A.1}$$

where N_v is the number of particles contained in volume V_m, and n_{p}^k is the number of physical particles represented by the kth computational particle.

In order to avoid complicated expressions arising from expressing the interpolation schemes in 3-D, only 1-D formulations are given with the reference to 1-D grid shown in Fig. 17. These expressions can be readily extended to three dimensions. In Fig. 17, m is the grid point index and c is the grid cell index.

LPI-2, LPI-4 and PCA can be expressed in a very general way for both forward interpolation and backward estimation. The formulation for TSE is slightly different and will be discussed separately. Fluid velocity $\{U^{\mathrm{f}}(X^k)\}_M$ at the kth particle's location, which belongs to cth cell, is given by the summation of product of fluid velocities at grid nodes $U^{\mathrm{f}}(x_m)$ and basis functions b_l^x or

$$\{U^{\mathrm{f}}(X^k)\}_M = \sum_{m=c-\mathscr{O}/2+1}^{c+\mathscr{O}/2} U^{\mathrm{f}}(x_m) b_l^x(\xi_l^k), \tag{A.2}$$

where $\mathscr{O}$ is the order of the scheme which is two for LPI-2 and four for both LPI-4 and PCA, $l = m - c + \mathscr{O}/2$, and ξ_l^k is the elemental coordinate that is defined for each scheme in the following subsections. The convention followed in the above equation numbers the basis functions from left to right. For example, if a particle is located in 5th cell (i.e. $c = 5$), then the fourth-order LPI-4 interpolation scheme will yield four non-zero basis functions b_1 through b_4, and the fluid velocity at particle location will have contributions from grid nodes 4 through 7 or $m = 4, 7$ in the above summation. Based on the convention followed, the basis function that adds the contribution of fluid velocity at 4th grid node is numbered 1 while the one for 7th grid node is numbered 4.

Similarly, a general expression for the mean interphase momentum transfer term $\{F_{x,m}^{\mathrm{fp}}\}$ at mth grid node is given by

$$\{F_{x,m}^{\mathrm{fp}}\} = \frac{1}{V_m}\sum_{c=m-\mathscr{O}/2}^{m+\mathscr{O}/2-1}\sum_{k=1}^{N^c} f_x^k n_{\mathrm{p}}^k b_l^x(\xi_l^k), \tag{A.3}$$

where N^c is the number of computational particles in cth cell, and all the other quantities have the same meaning as before. To clarify the above equation, consider the case of a fourth ordered scheme. From Fig. 17, the estimate for $\{F_{7,x}^{\mathrm{fp}}\}$ will include the contribution from particles located in cells 5–8. The above method for estimating the mean interphase momentum transfer has been widely used in simulation of particle-laden flows. For example, Boivin et al. (1998) uses the second-order linear interpolation (LPI-2), and Sundaram and Collins (1996) uses the fourth-order Lagrange polynomial interpolation (LPI-4) scheme.

The next three subsections that follow defines the basis functions for LPI-4, LPI-2, and PCA. In addition, the last subsection completely describes the two-stage estimation (TSE) algorithm which so far has not been explained.

A.1. Linear interpolation (LPI-2)

LPI-2 is a second-order scheme. For a point x that lies in the interval $[x_m, x_{m+1}]$, it has two linear basis functions

$$b_1^x = 1 - \xi, \quad b_2^x = \xi, \tag{A.4}$$

where ξ is the elemental coordinate defined as

$$\xi = \xi_1 = \xi_2 = \frac{x - x_m}{x_{m+1} - x_m}. \tag{A.5}$$

A.2. Lagrange polynomial interpolation (LPI)

LPI-4 is a fourth-order scheme and has four cubic polynomials as basis functions. For a point x lying in the interval $[x_m, x_{m+1}]$ on a structured grid with constant grid spacing, the four basis functions are

$$\begin{aligned} b_1^x &= -\frac{1}{6}(\xi)(\xi-1)(\xi-2), \\ b_2^x &= \frac{1}{2}(\xi-1)(\xi+1)(\xi-2), \\ b_3^x &= -\frac{1}{2}(\xi)(\xi+1)(\xi-2), \\ b_4^x &= \frac{1}{6}(\xi)(\xi+1)(\xi-1), \end{aligned} \tag{A.6}$$

where ξ is the elemental coordinate defined as

$$\xi = \xi_1 = \xi_2 = \xi_3 = \xi_4 = \frac{x - x_m}{x_{m+1} - x_m}. \tag{A.7}$$

These basis functions are non-zero over the entire interpolation stencil that spans the interval $[x_{m-1}, x_{m+2}]$. They are shown in Fig. 2a.

A.3. Piecewise cubic approximation (PCA)

PCA is a fourth-order scheme and has four *piecewise* cubic polynomials as basis functions. For a point x lying in the interval $[x_m, x_{m+1}]$ on a structured grid with constant grid spacing, the four basis functions are

$$\begin{aligned} b_1^x &= \frac{1}{6}(2+\xi_1)^3, \quad \xi_1 = \frac{x_{m-1} - x}{h} \quad \text{for } -2 \leqslant \xi_1 < -1, \\ b_2^x &= \frac{1}{6}(-3\xi_2^3 - 6\xi_2^2 + 4), \quad \xi_2 = \frac{x_m - x}{h} \quad \text{for } -1 \leqslant \xi_2 < 0, \\ b_3^x &= \frac{1}{6}(3\xi_3^3 - 6\xi_3^2 + 4), \quad \xi_3 = \frac{x_{m+1} - x}{h} \quad \text{for } 0 \leqslant \xi_3 < 1, \\ b_4^x &= \frac{1}{6}(2-\xi_4)^3, \quad \xi_4 = \frac{x_{m+2} - x}{h} \quad \text{for } 1 \leqslant \xi_4 \leqslant 2, \end{aligned} \tag{A.8}$$

where ξ_1, ξ_2, ξ_3, ξ_4 are the elemental coordinates defined distinctively for each basis function. It is to be noted that unlike in LPI-4, the basis functions for PCA are defined only piecewise. Fig. 2 shows these basis functions which are non-zero in the interval $[x_m, x_{m+1}]$.

A.4. Two-stage estimation algorithm

The TSE algorithm constructs a piecewise-polynomial approximation $\tilde{\phi}(x)$ to a mean field $\langle\phi(x)\rangle$ from particle data ϕ^l given at locations X^l. It was originally developed by Dreeben and Pope (1992) for application to PDF methods, and has the advantage of working with unstructured grids also. It is being reproduced here for completeness. In this algorithm, the first stage constructs estimates at knots (center of mass locations of the particle data) using top-hat or linear basis functions (LPI-2). These first-stage estimates are then used as

weighted data for the second stage in which a local least-squares algorithm is implemented to fit a linear or quadratic polynomial. The details for each stage are given in the next two subsections.

A.4.1. Stage 1

The following quantities are defined in the first stage: The weight of the particles which support the mth grid node,

$$w(x_m) = \sum_{c=m-1}^{m} \sum_{l=1}^{N^c} \mu^l b^x_{m-c+1}; \tag{A.9}$$

the center of mass of particles which support the mth grid node,

$$\overline{X}(x_m) = \frac{\sum_{c=m-1}^{m} \sum_{l=1}^{N^c} X^l \mu^l b^x_{m-c+1}}{w(x_m)}; \tag{A.10}$$

and finally the estimate of the particle property at the center of mass,

$$\bar{\phi}(x_m) = \frac{\sum_{c=m-1}^{m} \sum_{l=1}^{N^c} \phi^l \mu^l b^x_{m-c+1}}{w(x_m)}, \tag{A.11}$$

where ϕ^l is called the particle property data. For mean interphase momentum transfer term estimation in $x-$ direction, the expression for ϕ^l is

$$\phi^l = f^l_x n(x_c, t),$$

where f_x is the particle force, and $n(x_c, t)$ is the particle number density at the center of the cth cell and it is computed as

$$n(x_c, t) = \frac{1}{V_c} \sum_{l=1}^{N^c} n^l. \tag{A.12}$$

A.4.2. Stage 2

In stage 2, a local least-squares algorithm is implemented to calculate an approximation to the mean field that minimizes error with respect to the knot estimates. The output from the first stage, $(\overline{X}(x_m), \bar{\phi}(x_m))$ along with the weights w_m forms the input for this stage. The objective of the local least-squares method is to provide an estimate for the mean field at the Eulerian grid node x_m by fitting a polynomial to data which lies within a neighborhood of x_m, the size of which is characterized by bandwidth, W. For each estimate, the data is weighted with a kernel Q, where

$$Q(u) \equiv \begin{cases} (1-u^2)^2, & |u| \leqslant 1, \\ 0, & \text{otherwise.} \end{cases}$$

If x_p is an Eulerian grid node, then $\tilde{\phi}(x_p)$ is a polynomial estimate for the underlying function in a neighborhood of x_m which minimizes the expression

$$\sum_m Q\left(\frac{\overline{X}(x_m) - x_p}{W}\right) w(x_m)[\tilde{\phi}(x_p) - \bar{\phi}(x_m)]. \tag{A.13}$$

The linear two-stage algorithm is implemented by fitting a first order polynomial to the points $(\overline{X}(x_m), \bar{\phi}(x_m))$ in a neighborhood within a distance W centered at the grid node x_p. We take a function of the form

$$\tilde{\phi}(x) = \tilde{a} + \tilde{b}(x - x_p),$$

where $\tilde{a}$ and $\tilde{b}$ are unknown constants to be determined. If

$$\widehat{X}_{mp} = \overline{X}(x_m) - x_p, \tag{A.14}$$

$$\widehat{Q}_{mp} = w(x_m) Q\left(\frac{\widehat{X}_{mp}}{W}\right), \tag{A.15}$$

then the constants $\tilde{a}$ and $\tilde{b}$ which minimize Eq. (A.13) are determined by solving the matrix equation

$$\begin{bmatrix} \sum_m \widehat{Q}_{mp} & \sum_m \widehat{Q}_{mp}\widehat{X}_{mp} \\ \sum_m \widehat{Q}_{mp}\widehat{X}_{mp} & \sum_m \widehat{Q}_{mp}\widehat{X}^2_{mp} \end{bmatrix} \begin{bmatrix} \tilde{a} \\ \tilde{b} \end{bmatrix} = \begin{bmatrix} \sum_m \widehat{Q}_{mp}\bar{\phi}_m \\ \sum_m \widehat{Q}_{mp}\bar{\phi}_m\widehat{X}_{mp} \end{bmatrix}. \tag{A.16}$$

Finally, the estimate for the mean field – which is mean interphase momentum transfer term in our case – at the Eulerian grid node x_m is

$$\tilde{\phi}(x_m) = \tilde{a}. \tag{A.17}$$

Appendix B. Details of error decomposition

B.1. Statistical error

In the statistical error definition given by Eq. (22), $\{\mathbf{F}^{\mathrm{fp}}_m\}_{N_{\mathrm{pc}},M}$ is an unbiased estimator of $\langle\{\mathbf{F}^{\mathrm{fp}}_m\}_{N_{\mathrm{pc}},M}\rangle$ but owing to finite sample size N_{pc}, it has statistical fluctuations measured by the variance σ_F^2 of $\{\mathbf{F}^{\mathrm{fp}}_m\}_{N_{\mathrm{pc}},M}$, which is given by Eq. (B.1). The scaling of statistical error with number of samples is given by Eq. (23), where c_F which scales as σ_F is referred to as the statistical error coefficient, and θ is a standardized normal variate.

$$\sigma_F^2 = N_{\mathrm{pc}}\,\mathrm{var}(\{\mathbf{F}^{\mathrm{fp}}_m\}_{N_{\mathrm{pc}},M}). \tag{B.1}$$

In the definition of statistical error given by Eq. (22), $\langle\{\mathbf{F}^{\mathrm{fp}}_m\}_{N_{\mathrm{pc}},M}\rangle$ is an unknown and is approximated by ensemble averaging $\{\mathbf{F}^{\mathrm{fp}}_m\}_{N_{\mathrm{pc}},M}$ over $\mathscr{M}$ independent but identical simulations, such that

$$\langle\{\mathbf{F}^{\mathrm{fp}}_m\}_{N_{\mathrm{pc}},M}\rangle \cong \langle\{\mathbf{F}^{\mathrm{fp}}_m\}_{N_{\mathrm{pc}},M}\rangle_{\mathscr{M}} = \frac{1}{\mathscr{M}}\sum_{i=1}^{\mathscr{M}}\{\mathbf{F}^{\mathrm{fp}}_m\}^{(i)}_{N_{\mathrm{pc}},M}. \tag{B.2}$$

Note that $\langle\{\mathbf{F}^{\mathrm{fp}}_m\}_{N_{\mathrm{pc}},M}\rangle_{\mathscr{M}}$ is itself a random variable with mean and variance given by

$$\langle\langle\{\mathbf{F}^{\mathrm{fp}}_m\}_{N_{\mathrm{pc}},M}\rangle_{\mathscr{M}}\rangle = \langle\{\mathbf{F}^{\mathrm{fp}}_m\}_{N_{\mathrm{pc}},M}\rangle, \tag{B.3}$$

$$\mathrm{var}(\langle\{\mathbf{F}^{\mathrm{fp}}_m\}_{N_{\mathrm{pc}},M}\rangle_{\mathscr{M}}) = \frac{1}{\mathscr{M}}\,\mathrm{var}(\{\mathbf{F}^{\mathrm{fp}}_m\}_{N_{\mathrm{pc}},M}) = \frac{\sigma_F^2}{\mathscr{M}N_{\mathrm{pc}}}. \tag{B.4}$$

If the statistical error due to finite number of realizations $\mathscr{M}$ is defined as

$$\Sigma_{F,\mathscr{M}} = \langle\{\mathbf{F}^{\mathrm{fp}}_m\}_{N_{\mathrm{pc}},M}\rangle_{\mathscr{M}} - \langle\{\mathbf{F}^{\mathrm{fp}}_m\}_{N_{\mathrm{pc}},M}\rangle, \tag{B.5}$$

then from the central limit theorem, the scaling of $\Sigma_{F,\mathscr{M}}$ with number of realizations is

$$\Sigma_{F,\mathscr{M}} = \mathscr{M}^{-1/2}\sigma_{F,\mathscr{M}}\xi, \tag{B.6}$$

where ξ is a standardized normal variate, and $\sigma_{F,\mathscr{M}}$ is the standard error which based on Eq. (B.4) can be written as

$$\sigma^2_{F,\mathscr{M}} = \mathscr{M}\,\mathrm{var}(\langle\{\mathbf{F}^{\mathrm{fp}}_m\}_{N_{\mathrm{pc}},M}\rangle_{\mathscr{M}}) = \frac{\sigma_F^2}{N_{\mathrm{pc}}}. \tag{B.7}$$

Therefore, the final form for $\Sigma_{F,\mathscr{M}}$ is

$$\Sigma_{F,\mathscr{M}} = \langle \{\mathbf{F}_m^{\mathrm{fp}}\}_{N_{\mathrm{pc}},M} \rangle_{\mathscr{M}} - \langle \{\mathbf{F}_m^{\mathrm{fp}}\}_{N_{\mathrm{pc}},M} \rangle = \frac{c_F \xi}{\sqrt{(\mathscr{M} N_{\mathrm{pc}})}}. \tag{B.8}$$

The total statistical error Σ_F can be rewritten as the summation of approximate statistical error denoted by $\widehat{\Sigma}_F$ and $\Sigma_{F,\mathscr{M}}$ (which is defined by above equation):

$$\Sigma_F = \widehat{\Sigma}_F + \Sigma_{F,\mathscr{M}}, \tag{B.9}$$

where the definition of approximate statistical error and its scaling with the number of samples and realizations is given by

$$\widehat{\Sigma}_F = \{\mathbf{F}_m^{\mathrm{fp}}\}_{N_{\mathrm{pc}},M} - \langle \{\mathbf{F}_m^{\mathrm{fp}}\}_{N_{\mathrm{pc}},M} \rangle_{\mathscr{M}} = \Sigma_F - \Sigma_{F,\mathscr{M}} = \frac{c_F \theta}{\sqrt{N_{\mathrm{pc}}}} - \frac{c_F \xi}{\sqrt{(\mathscr{M} N_{\mathrm{pc}})}}. \tag{B.10}$$

References

Are, S., Hou, S., Schmidt, D., 2005. Second-order spatial accuracy in Lagrangian–Eulerian spray calculations. Numer. Heat Transfer, Part B 48, 25–44.

Balachandar, S., Maxey, M.R., 1989. Methods for evaluating fluid velocities in spectral simulations of turbulence. J. Comput. Phys. 83, 96–125.

Boivin, M., Simonin, O., Squires, K.D., 1998. Direct numerical simulation of turbulence modulation by particles in isotropic turbulence. J. Fluid Mech. 375, 235–263.

Conte, S.D., Boor, C.d., 1980. Elementary Numerical Analysis: An Algorithmic Approach, third ed.. In: International Series in Pure and Applied Mathematics McGraw-Hill, p. 51 (Chapter 2).

Crowe, C.T., 1982. Review-numerical models for dilute gas-particle flows. ASME J. Fluids Eng. 104, 297–303.

Dreeben, T.D., Pope, S.B., 1992. Nonparametric estimation of mean fields with application to particle methods for turbulent flows. Tech. Rep. FDA 92-13, Sibley School of Mechanical and Aerospace Engineering, Cornell University, Ithaca, NY 14853, November.

Drew, D.A., Passman, S.L., 1998. Theory of Multicomponent Fluids. In: Applied Mathematical Sciences. Springer, New York.

Elghobashi, S.E., Truesdell, G.C., 1993. On the two-way interaction between homogeneous turbulence and dispersed solid particles. I: Turbulence modification. Phys. Fluids A 5, 1790–1801.

Evans, M., Harlow, F.H., 1957. Hydrodynamic problems involving large fluid distortions. J. Assoc. Comput. Mach. 4, 137–142.

Harlow, F.H., 1988. PIC and its progeny. Comput. Phys. Commun. 48, 1–10.

Lakehal, D., Narayanan, C., 2003. Numerical analysis of the continuum formulation for the initial evolution of mixing layers with particles. Int. J. Multiphase Flow 29, 927–941.

Monaghan, J., 1992. Smoothed particle hydrodynamics. Annu. Rev. Astron. Astrophys. 30, 543–574.

Monaghan, J., Lattanzio, J., 1985. A refined particle method for astrophysical problems. Astron. Astrophys. 149, 135–143.

Narayanan, C., Lakehal, D., Yadigaroglu, G., 2002. Linear stability analysis of particle-laden mixing layers using particle tracking. Powder Technol. 125, 122–130.

Pope, S.B., 1995. Particle method for turbulent flows: integration of stochastic model equations. J. Comput. Phys. 117 (2), 332–349.

Pope, S.B., 2000. Turbulent Flows. Cambridge University Press, Port Chester, NY, pp. 11–12 (Chapter 1).

Squires, K.D., Eaton, J.K., 1990. Particle response and turbulence modification in isotropic turbulence. Phys. Fluids A 2, 1191–1203.

Subramaniam, S., 2000. Statistical representation of a spray as a point process. Phys. Fluids 12 (10), 2413–2431.

Subramaniam, S., 2001. Statistical modeling of sprays using the droplet distribution function. Phys. Fluids 13 (3), 624–642.

Subramaniam, S., Haworth, D.C., 2000. A Pdf method for turbulent mixing and combustion on three-dimensional unstructured deforming meshes. J. Engine Res. 1 (2), 171–190.

Sundaram, S., Collins, L.R., 1996. Numerical considerations in simulating a turbulent suspension of finite-volume particles. J. Comput. Phys. 124, 337–350.

Sundaram, S., Collins, L.R., 1999. A numerical study of the modulation of isotropic turbulence by suspended particles. J. Fluid Mech. 379, 105–143.

Welton, W., Pope, S.B., 1997. PDF model calculations of compressible turbulent flows using smoothed particle hydrodynamics. J. Comput. Phys. 134 (1), 150–168.

Xu, J., Pope, S.B., 1999. Assessment of numerical accuracy of PDF Monte Carlo methods for turbulent reacting flows. J. Comput. Phys. 152 (1), 192–230.

Yeung, P.K., Pope, S.B., 1988. An algorithm for tracking fluid particles in numerical simulation of homogeneous turbulence. J. Comput. Phys. 79, 373–416.